Rheologica Acta (2026) 65:503–523
https://doi.org/10.1007/s00397-026-01567-6

ORIGINAL CONTRIBUTION

Anionic collagen processed by alkaline hydrolysis: rheological, biological, and 3D printability assessment

Lívia C. Massimino[1,2] · Mirella R. V. Bertolo-Cagnoto[3] · Larissa Tessaro[4] · Virginia da C. A. Martins[4] · Bianca Chieregato Maniglia[4] · Ana Maria de G. Plepis[1,4] · Monica B. Mathor[1]

Received: 19 January 2026 / Revised: 13 March 2026 / Accepted: 24 March 2026 / Published online: 13 April 2026

Abstract

Collagen is the most abundant structural protein in the extracellular matrix, and its biocompatibility can be enhanced by chemical modification into a negatively charged matrix. This study investigates the effect of alkaline hydrolysis time (24, 48, 72, and 96` h) on the rheological behavior and processability of anionic concentrated collagen solutions extracted from bovine tendon. By systematically modulating hydrolysis time, we demonstrate how increasing negative charge density drives a rearrangement of the collagen network, resulting in more elastic and shear-thinning behavior, as evidenced by higher storage moduli, increased zero-shear viscosity, and enhanced creep-recovery response. Among the tested formulations, the 72-h hydrolyzed collagen exhibited the most balanced rheological profile and enabled extrusion-based 3D printing with high fidelity, achieving geometry preservation of 104 ± 4% (star angle), 98 ± 2% (scaffold area), and effective macroporosity of 84%. Longer hydrolysis led to decreased scaffold pore size and increased absorption of phosphate-buffered saline. All materials were non-cytotoxic and supported cell adhesion (58.74—74.89%). Overall, this work highlights how rheological characterization can guide the design and processability of collagen-based bioinks, linking structural and mechanical properties to 3D printing performance and biological outcomes.

Graphical Abstract

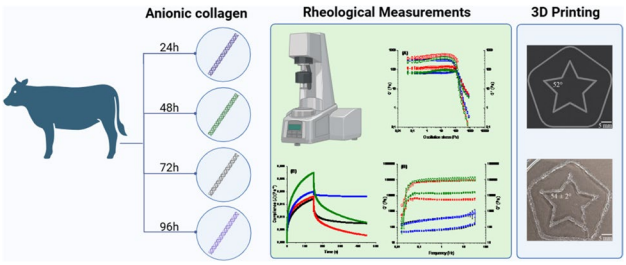

Keywords Biopolymers · Rheology · Biocompatible scaffolds · BALBC-3T3 · 3D printing

Lívia C. Massimino and Mirella R. V. Bertolo-Cagnoto contributed equally to this work.

✉ Mirella R. V. Bertolo-Cagnoto
mirella.bertolo@usp.br

[1] Nuclear and Energy Research Institute (IPEN-CNEN/SP), São PauloSP, Brazil

[2] University of São Paulo (USP), Interunits Graduate Program in Bioengineering (EESC/FMRP/IQSC), São Carlos, SP, Brazil

[3] Luiz de Queiroz College of Agriculture (ESALQ), University of São Paulo (USP), Piracicaba, SP, Brazil

[4] University of São Paulo (USP), São Carlos Institute of Chemistry (IQSC), São Carlos, SP, Brazil

Introduction

Natural polymers, like collagen, are commonly used to obtain scaffolds for tissue engineering applications (Wang et al. 2023). Collagen is an abundant and natural biopolymer, being the most abundant structural protein in extracellular matrix; type I accounts for more than 80% of all types of collagens (Sun et al. 2018; Bazrafshan and Stylios 2019; Figueiredo et al. 2025). Collagen-based tissues are organized on the smallest length scale into hierarchical structures with triple-helical collagen molecules, where parts of it are sequences of $(Gly\text{-}X\text{–}Y)_{n.}$ While Gly corresponds to glycine, X and Y are often proline and hydroxyproline, respectively (Gautieri et al. 2011; Amirrah et al. 2022).

Collagen presents many interesting physical and chemical properties, like its unique triple helix structure, low immunogenicity, good biocompatibility, and flexibility (Amirrah et al. 2022; Wang et al. 2023). These properties play an important role in the use of this biopolymer as a biomaterial in many areas, including wound healing, tissue regeneration, and bioprinting (Liu et al. 2019; Fan et al. 2023; Wang et al. 2023; Moss et al. 2025). Depending on the desired application, collagen can be used in its native or reconstituted form or suffer modification by chemical, physicochemical or enzymatic processes, generating a positively or negatively charged matrix, which modifies its mechanical properties and biocompatibility (Bet et al. 2001; Zhang et al. 2005).

The increase in the number of negative charges can generate small changes in collagen structure like the pore size due to the electrostatic repulsion caused between them; moreover, its biocompatibility is increased, and the inflammatory response is reduced (Bet et al. 2001; Munhoz et al. 2018). One of the processes applied for obtaining anionic collagen is the alkaline hydrolysis of the carboxamide groups of the amino acid residues asparagine and glutamine, which are present in the α chains of tropocollagen (Bet et al. 2001). The selective hydrolysis reaction promotes, depending on the reaction time, a total increase of up to 134 loads per unit of tropocollagen, changing the pattern of organization of the microfibrillar structure of the collagen matrix, due to the disruption of the tissue crosslinks and to the new pattern of electrostatic interactions (Bet et al. 2001).

The advancement of biofabrication technologies, particularly extrusion-based 3D printing, has enabled the production of three-dimensional scaffolds with precise control over architecture, porosity, and interconnectivity, factors that are critical for nutrient diffusion, cell migration, and new tissue formation (Xie et al. 2024). The injectability and self-healing abilities of collagen solutions are essential for bioprinting, as they govern the extrusion, stacking, and structural integrity of bioprinted materials (Ju et al. 2025). However, the success of these systems is directly conditioned by the rheological and structural properties of the biomaterial employed.

The rheological behavior of collagen systems is closely related to their structural organization in solution. Depending on concentration and physicochemical conditions, collagen may behave either as a concentrated polymer solution dominated by molecular entanglements or as a physical gel formed through fibrillar self-assembly. In entangled collagen solutions, viscoelasticity arises mainly from transient intermolecular interactions, typically leading to frequency-dependent storage (G') and loss (G") moduli. In contrast, fibrillar collagen gels exhibit a more solid-like response with weak frequency dependence of the viscoelastic moduli and a dominant elastic component. Classical studies on collagen gelation, particularly those by Djabourov et al. (1993), demonstrated that the transition from solution to gel is associated with the formation of a percolated fibrillar network and characteristic rheological signatures described by gelation theory, such as the Winter-Chambon criterion. Understanding these rheological regimes is important for interpreting the viscoelastic behavior of collagen systems and for predicting their processability in applications such as extrusion-based bioprinting.

However, the rheological properties of collagen are highly sensitive to its structural integrity and molecular aggregation state, which are both influenced by extraction conditions. Insufficient extraction times may result in low collagen solubilization, whereas excessive extraction times can decrease thermal stability and lead to a gradual loss in the ability of collagen molecules to form fibrils, with increasing carboxyl content (Bet et al. 2001).

The use of various types of collagens in tissue engineering is well established; however, there is a gap in information regarding the rheological, physicochemical, and biological properties of anionic collagen and how they are affected by its extraction process. Therefore, the aim of this study was to investigate the influence of four different alkaline hydrolysis durations (24, 48, 72, and 96 h) on the rheological properties and cell adhesion characteristics of collagen materials intended for use in tissue engineering. Additionally, 72 h hydrolyzed collagen was tested as a proof-of-concept ink to assess the feasibility of using this material in 3D printing applications. This research provides new insights into anionic collagen and explores how its extraction via alkaline hydrolysis may affect the rheology and development of scaffolds for tissue growth.

The findings of this study could serve as a foundation for future research on the application of anionic collagen materials in tissue engineering and 3D bioprinting. Unlike

previous studies that primarily report isolated physicochemical or biological properties of anionic collagen, this work provides a systematic structure–rheology–printability correlation as a function of alkaline hydrolysis time. By integrating oscillatory and steady-shear rheology with printability assessment and early biological evaluation, we identify an intermediate hydrolysis window (72 h) that balances network integrity, shear-thinning behavior, and partial structural recovery, enabling extrusion-based 3D printing with enhanced geometric fidelity. Rather than proposing a formulation-specific solution, this study introduces a rheology-driven design framework for collagen-based bioinks.

Materials and methods

The bovine tendon used to obtain collagen was acquired from the local market (São Carlos – SP, Brazil). All reagents used were of PA grade and used as such.

Preparation of anionic concentrated collagen solutions by alkaline hydrolysis

Concentrated collagen solutions were prepared by the treatment of bovine tendon at room temperature with an alkaline solution containing chlorides and sulfate salts and bases of alkaline and alkaline earth metals for 24, 48, 72 and 96 h (Horn and Martins 2009), and were named Col 24, Col 48, Col 72, and Col 96, respectively. After that, the materials were equilibrated with a solution containing chlorides and sulfates of sodium, calcium and potassium for a 6 h period. Excess salts were removed by washing with a 3% (w/w) boric acid solution, deionized water, a 0.3% (w/w) EDTA solution pH 11.0, and deionized water one more time. The resulting collagen was extracted with an aqueous solution of acetic acid pH 3.5 and homogenized. The concentration of the concentrated collagen solution was determined by lyophilization and adjusted to 1.0% (w/w) with a pH 3.5 acetic acid solution.

The concentrated collagen solutions obtained at different hydrolysis times were characterized in terms of their rheological properties and printability (described in the next section). Part of them were placed in Teflon molds, frozen in liquid nitrogen and lyophilized to obtain collagen scaffolds. Neutralization of these scaffolds was performed in ammonia vapor for 8 h. The scaffolds were also named S_Col 24, S_Col 48, S_Col 72, and S_Col 96, corresponding to each time point of hydrolysis. These samples were used for the characterization of anionic collagen-based scaffolds and in vitro assays. Table 1 provides an overview of the nomenclature used for each sample according to their preparation method.

Table 1 Overview of sample identification: hydrolysis times and preparation methods for each testing procedure

Hydrolysis times	Concentrated collagen solutions sample	Lyophilized scaffold sample	3D print sample
24 h	Col 24	S_Col 24	-
48 h	Col 48	S_Col 48	-
72 h	Col 72	S_Col 72	Col 72
96 h	Col 96	S_Col 96	-

Characterization of anionic concentrated collagen solutions

Rheological properties

Rheological properties of the concentrated collagen solutions were carried out in an AR-1000N controlled strain rheometer (TA Instruments, New Castle, USA) with a stainless-steel plate cone geometry (20 mm diameter, 2° angle, 69 μm gap) and a Peltier system for temperature control. Rheological data was collected and analyzed by the software Rheology Advantage (TA Instruments, New Castle, USA).

Dynamic oscillatory tests

Stress controlled amplitude sweep measurements Stress controlled amplitude sweep measurements were performed from 0.05 to 1000 Pa, at 1.0 Hz and 25 °C. From the curves of the elastic (G') and viscous (G'') moduli as a function of oscillation stress, the linear viscoelastic region (LVE) could be determined, as well as the following parameters: the critical deformation ($\gamma_{L,}$ %), *i.e.*, the highest % strain applied before the solution leaves LVE; the yield stress ($\tau_{y,}$ Pa), the corresponding shear stress at γ_L; G'_{LVE} (Pa), the elastic modulus value at the limit of LVE; tan δ = G''/G'; G' = G'' (Pa), the moduli value at their intersection; and the flow point (τ_f, Pa), the shear stress value when G' = G'' (Razmkhah et al. 2017).

Frequency sweep measurements Frequency sweep measurements were performed from 0.03 to 80 Hz at 1% strain and 25 °C. The parameters determined from these measurements were the complex viscosity (η*, Pa s) at 1 Hz, as well as the slope of η* (determined from the linear adjustment of η* curves from 0.03 to 30 Hz).

Temperature sweep measurements Temperature sweep measurements were performed to evaluate the viscoelastic behavior of the collagen solutions as a function of temperature. The storage (G′) and loss (G″) moduli were measured from 20 to 55 °C at 1% strain and 1.6 Hz, and the complex

viscosity (η*) was calculated from the viscoelastic moduli and used to analyze the temperature dependence of the system.

Steady shear tests

The steady shear measurements were conducted from 0.1 to 1000 s^{-1} at 25 °C. Cross model (Eq. 1) was applied for the adjustment of the curves (from 0.1 s^{-1}). In the equation, η_0 and η_∞ are the viscosities at zero shear and infinite shear (Pa s), respectively, $\dot{\gamma}$ is the shear rate (s^{-1}), k is the consistency index (s), and n is the rate index (dimensionless).

$$\frac{\eta - \eta_\infty}{\eta_0 - \eta_\infty} = \frac{1}{(1 + (k\dot{\gamma})^n)} \quad (1)$$

Creep-recovery tests

Creep-recovery measurements were carried out to identify any modifications in the internal structure of the collagen solutions, caused by the application of a fixed stress for a certain period of time (Yang et al. 2018). In the retardation (creep) step, the solutions were subjected to a shear stress of 10 Pa for 150 s; then, the deformation was removed, and the solutions were able to recover for 300 s in the recovery step. Experimental data were expressed using the compliance (J(t)), from J(t)=γ(t)/σ, where γ is the shear strain, σ is the applied shear stress, and t is time). The % of recovered compliance of the collagen solutions was calculated according to Eq. (2), in which J_{100} and J_{450} are the compliance values at 100 s and 450 s, respectively.

$$\%\ recovered\ compliance = \left(\frac{J_{100} - J_{450}}{J_{100}}\right) x100 \quad (2)$$

3D printability

Based on rheological screening of all formulations, Col 72 was selected as a proof-of-concept bioink for extrusion-based printing due to its elastic strength, shear-thinning behavior, and partial structural recovery. In contrast, the formulations obtained at other hydrolysis times exhibited a markedly more fibrillar and heterogeneous microstructure. This structural organization significantly compromised the extrusion process, as the presence of fibrous aggregates impaired homogeneous flow through the nozzle, increased flow resistance, and led to intermittent filament formation and poor deposition control. As a result, these formulations did not allow stable and continuous extrusion under the tested printing conditions, making them unsuitable for a reliable printability assessment within the scope of this study.

Col 72 was prepared as described in Section Preparation of anionic concentrated collagen solutions by alkaline hydrolysis and subsequently used for 3D printing experiments. Star-shaped structures without infill (42 × 42 mm, two layers) and scaffolds (20 × 20 × 0.8 mm) with 30% infill, a rectangular infill pattern, and four layers were printed using a modular extrusion-type 3D bioprinter (bioV4-BioEdPrinter v4-4, BioEdTech, Sao Paulo, SP, Brazil). The shapes were printed, at room temperature, according to the following parameters: robotic arm speed = 10 mm/s; extrusion flow (w) = 100%; needle diameter (d) = 1.2 mm. Three samples for each shape were printed (Sponchiado et al. 2024). Photographs of the surface stars and scaffolds were captured in triplicate using an Samsung Galaxy A54 (Samsung Electronics, Suwon, South Korea) and the images were analyzed by ImageJ software (version 1.54 g bundled with 64-bit Java 1.8.0, January 2026).

Image acquisition was performed under standardized conditions, including controlled LED illumination, a fixed distance between the camera and the sample, and a uniform white background. A metric ruler was positioned alongside the samples in each image to provide a spatial scale for calibration and dimensional analysis. All photographs were taken inside a light-controlled box to minimize shadow formation and reduce variability caused by external light interference. Geometry fidelity (GF) was calculated by comparing the angles of the 3D-printed star-shaped structures with those of the corresponding 3D digital model (52°) (Eq. 3), and by comparing the filament width (mm) with the needle diameter (1.2 mm) (Eq. 4), as well as by comparing the area of the 3D-printed scaffold (mm^2) with that of the corresponding digital scaffold model (314 mm^2) (Eq. 5). Effective macroporosity (EM) was calculated by comparing the number of macropores (N) in the 3D-printed scaffold with the number of macropores in the digital scaffold model (32) (Eq. 6).

$$GF\ star\ angle\ (\%) = \left(\frac{angle\ of\ 3D\ printed\ star}{angle\ of\ 3D\ digital\ model}\right) x100 \quad (3)$$

$$GF\ filament\ width\ (\%) = \left(\frac{filament\ width\ of\ 3D\ printed\ star}{needle\ diameter}\right) x100 \quad (4)$$

$$GF\ scaffold\ area\ (\%) = \left(\frac{area\ of\ 3D\ printed\ star}{area\ of\ 3D\ digital\ model}\right) x100 \quad (5)$$

$$EM\ scaffold\ (\%) = \left(\frac{N\ 3D\ printed\ scaffold}{N\ 3D\ digital\ model}\right) x100 \quad (6)$$

Characterization of anionic collagen-based scaffolds

Thermal properties by differential scanning calorimetry (DSC)

The denaturation temperature of collagen present in the scaffolds was obtained by differential scanning calorimetry (DSC) using a DSC Q10 (TA Instruments). The analysis was performed under N_2 atmosphere using 20 mg of sample, a temperature range from 10 to 120 ºC and a heating rate of 10 ºC min^{-1}.

Functional groups by fourier transform infrared spectroscopy – attenuated total reflectance (FTIR–ATR)

The hydrolyzed collagens were placed in Teflon® molds and dried under air flow in order to form films by the casting method. The characteristic bands of collagen in the films were analyzed in Bruker Alpha Platinum-ATR equipment, in a range of 4000–400 cm^{-1}, with 64 scans and a resolution of 2 cm^{-1}.

Morphology by scanning electron microscopy (SEM) and pores size

The scaffold morphology was observed using a FEG-SEM JEOL JSM-7200F equipment. Prior the analysis, the scaffolds were bonded in stubs with conductive carbon tape and covered with 6 nm a gold layer (BAL-TEC, Liechtenstein, Germany), with a chamber pressure of 2.00×10^{-2} mbar, a 60 mA current and a 0.60 nm s^{-1} deposition rate. The software ImageJ® was used to measure the size of scaffold pores ($n = 30$). Transversal sections were obtained on a LEO 440 equipment (LEO Electron Microscopy Ltda), with an Oxford detector (Oxford Instruments Inc.), using a 20 kV beam. The samples were previously coated with 20 nm of gold in a Balsers model SDC 050 metalizer.

Porosity

The porosity of the scaffolds was determined following the procedure used by Garcia et al. (2021). The scaffolds were placed in a chamber in the presence of $NaOH_{(s)}$ for 24 h. Their dimensions were measured with a micrometer M110-25 (Mitutoyo Mfg. Co.), and the dry volumes of the scaffolds were calculated (V_1). Then, the scaffolds were placed in 5 mL of ethanol (which was previously weighed, W_1). After 24 h the scaffolds were removed, and the remaining ethanol was weighed again (W_2). The procedure was performed in quintuplicate for each sample and the porosity was calculated according to the Eq. (7), in which ρ_{EtOH} is the ethanol density (0.79 g mL^{-1}).

$$\% \; porosity = \left(\frac{\frac{(W_1 - W_2)}{\rho_{EtOH}}}{V_1} \right) x100 \tag{7}$$

PBS absorption and kinetic models

PBS (pH 7.4) absorption assays were performed in triplicate. The scaffolds were placed in a chamber in the presence of $NaOH_{(s)}$ for 24 h. After drying, the scaffolds were weighed (W_{dry}), placed in a PBS buffer, and reweighed at specific time intervals (W_{wet}). At the end, the percentage of buffer absorbed by the scaffold was calculated using Eq. (8).

$$\% \; PBS \; absorption = \left(\frac{W_{wet} - W_{dry}}{W_{dry}} \right) x100 \tag{8}$$

In vitro assays

The scaffolds were irradiated in a Cobalt-60 Multipurpose Gamma Irradiator, at Nuclear and Energy Research Institute (IPEN/CNEN) in Sao Paulo. The dose was 15 kGy.

(5 kGy h^{-1}) and it was determined after previous studies (Massimino et al. 2020), which verified the appropriate irradiation dose according to the lack of morphological alterations in the materials. The irradiation protocol was based on the International Organization for Standardization 11,137 (2017).

In the biological tests, the cell line Balbc-3T3 (CCL-163, ATCC) was used. The cell line was maintained on appropriate cell culture media, Dulbecco's Modified Eagle Medium (DMEM) (Gibco, Invitrogen) with 10% bovine fetal serum (Gibco, Invitrogen), at 37 °C and 5% CO_2 humid atmosphere.

MTS cytotoxicity assay

Extracts of the scaffolds were prepared in order to assess the hazard potential of the samples, with the extraction conditions being selected, according to the International Organization for Standardization 10,993 – part 12 (2012). Sterilized scaffolds were put into containers, and DMEM was added at a ratio of 0.1 g mL^{-1} (mass of scaffold per volume of DMEM). Then, the samples were incubated in 5% CO_2, at 37 °C for 24 h, after which the scaffolds were removed from the media and 100% extracts were obtained. All extracts were used immediately after preparation to prevent sorption onto the extraction container or any other changes in composition. Cells in culture medium (1×10^6 cells mL^{-1}) were exposed to S_Col 24, S_Col 48, S_Col 72 and S_Col 96 extracts. The plates were incubated for 24 h, at 37 °C and 5% CO_2. After this period, the supernatant was removed, and the cells were exposed to MTS (3- (4,5-dimethylthiazol-2-yl)−5-(3-carboxymethoxyphenyl)−2-(4-sulfophenyl)−2H-

tetrazolium)/PMS (phenazine methosulfate) solution (1 mg mL^{-1}) and incubated at 37 °C for 4 h. The optical density was determined using a spectrophotometer at 490 nm. Cell viability was calculated as a percentage of total cells, assuming the negative control to be 100% viable.

Cell adhesion assay

Alamar Blue® (Thermo Fisher Scientific) reagent was used to evaluate cell adhesion on the scaffolds based on the literature with modifications (Low et al. 2006). Each scaffold was transferred to a new 24-well plate (Nunclon, Nunc, CAT N° 142,475) and hydrated with 100 µL of cell culture media. Then, 100 µL of cell suspension (8×10^5 cells mL^{-1}) were added and incubated at 37 °C for 1 h. After that, 400 µL of cell media were added and incubated at 37 °C for 24 h. After incubation, the scaffolds were transferred to a new 24-well plate (Nunclon, Nunc, CAT N° 142,475) and 400 µL of the reagent Alamar Blue (diluted 1:10 in culture medium) was added and incubated overnight to ensure the reach of the entire scaffold. A volume of 100 µL of metabolized resazurin from each scaffold was transferred in triplicate into 96 well-microplates and fluorescence intensity was measured (excitation at 560 nm and emission at 590 nm) (SpectraMAx i3, Molecular Devices). A monolayer of cells was used as control. Unseeded scaffolds, incubated under the same culture conditions, were employed as negative controls, and the fluorescence values obtained for these scaffolds were subtracted from the sample results.

Statistical analysis

Quantitative data are presented as the mean ± standard deviation (SD). All analyses were performed in triplicate. Statistical analyses were performed by one-way ANOVA or Student's t-test. $p \leq 0.05$ was considered significant between two groups of data.

Results

The concentrated collagen solutions obtained at different hydrolysis times exhibited a homogeneous appearance, and the corresponding dried scaffolds formed porous structures.

Characterization of anionic concentrated collagen solutions

Rheological measurements

Dynamic oscillatory tests

Stress-controlled amplitude sweep measurements All collagen solutions, regardless of hydrolysis time (24–96 h), exhibited G'>G" within the LVE, the curves were model response typical of structured or concentrated polymer solutions (Fig. 1A). With LVE end and the increase in the applied strain, G' and G" moduli crossed, indicating the disruption of the polymeric network and its reversion to a liquid-like behavior, with G">G'.

The first parameter presented in Table 2 is the critical strain (γ_L), *i.e.*, the highest % of strain to which the solutions were subjected before their LVE ended. A higher γ_L indicates a wider linear viscoelastic region. The increase in the hydrolysis time seemed not to have affected the critical strain of collagen solutions: although Col 72 had the lowest γ_L (3.23 ± 0.62%), the increase from 24 h (4.69 ± 0.32%) to 96 h (4.17 ± 0.73%) of extraction did not statistically affect this parameter. Conversely, the yield stress (τ_γ), which represents the oscillation stress value for γ_L, was statistically the same for all the collagen solutions, regardless of the hydrolysis time.

The third parameter of Table 2 is the G' value at the limit of LVE, an indication of the highest elastic resistance within the linear viscoelastic region. G'_{LVE} varied with the hydrolysis time of the solutions and ranged from 342.02 ± 22.86 Pa (Col 24) to 417.63 ± 72.27 Pa (Col 96), but the difference between the samples was only significant ($p < 0.05$) for Col 72 solution, the sample with the highest structural strength (497.10 ± 90.68 Pa). The increase in hydrolysis time increased the number of negative charges present in solution, as it will be discussed in the following characterization assays, which may be leading to a rearrangement of the three-dimensional collagen network towards more elastic solutions.

The fourth parameter, loss tangent or tan δ, is the ratio between the viscous and the elastic moduli at the LVE limit; solutions with tan δ > 1.0 can be classified as viscous (since G">G'), while solutions with tan δ < 1.0 are considered elastic. If tan δ is between 0.1 and 1.0, the solution can also be classified as a concentrated polymeric solution, and not a true gel, as is the case of all collagen solutions of this study (Mandala et al. 2004).

G'=G" parameter indicates the value of the moduli when they cross and when the liquid-like behavior of the samples starts. The increase in hydrolysis time led to solutions with lower G'=G" values that ranged from 110.2 ± 3.39 Pa (Col 24) to 60.39 ± 4.64 Pa (Col 96). Accordingly, the flow point (τ_f) is the oscillation stress value when G'=G" and the solution starts to flow. Col 72 presented the highest τ_f (149.37 ± 13.30 Pa), almost 60 Pa higher than the one of Col 24 (91.76 ± 3.52 Pa); that result may be related to the higher rigidity of this solution, as pointed out by its G'_{LVE} value.

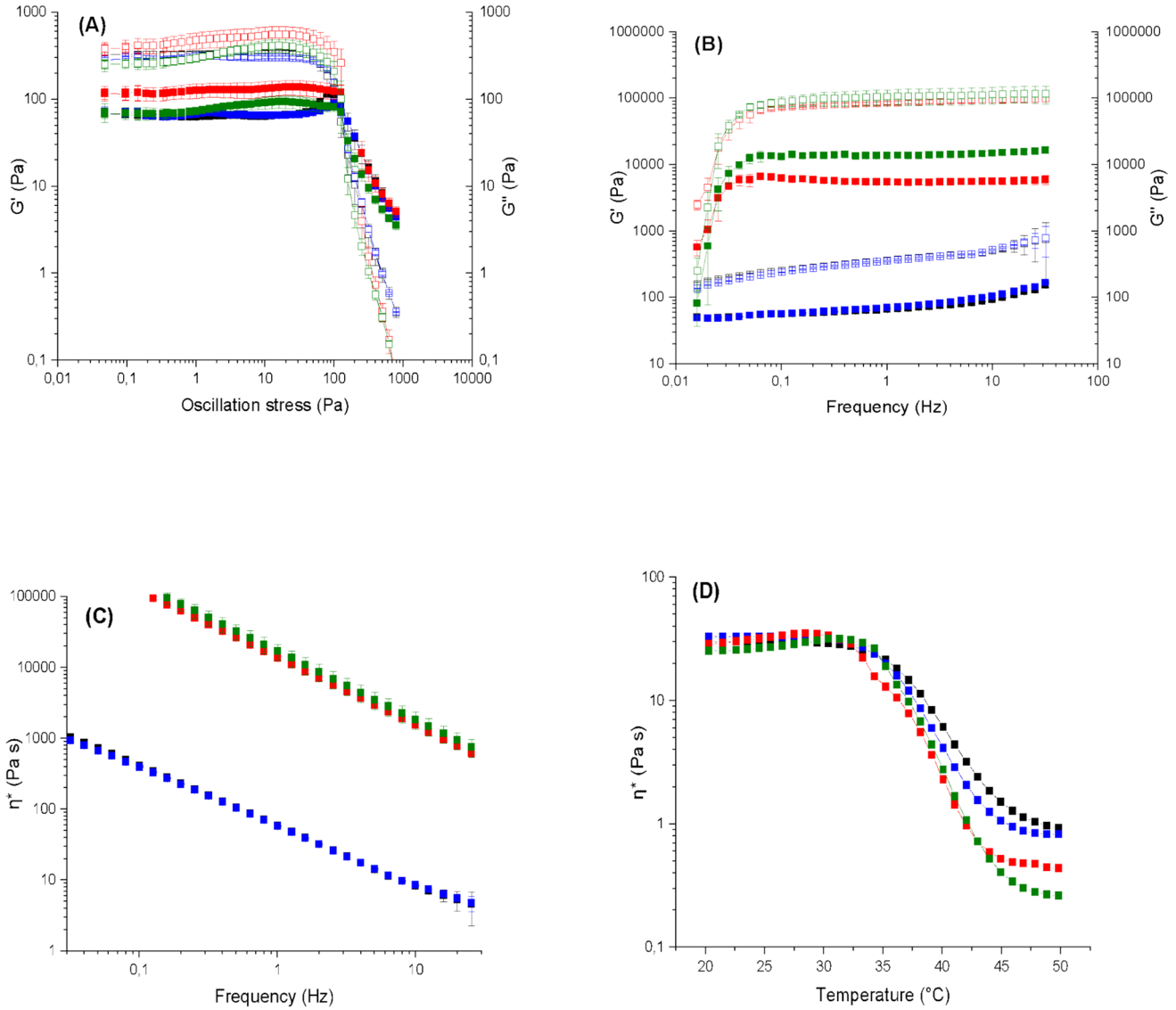

Fig. 1 **A** Elastic and viscous moduli against oscillation stress (Pa); **B** Elastic and viscous moduli as a function of frequency (Hz); **C** complex viscosity (η^*) as a function of frequency (Hz); **D** Complex viscosity (η^*) as a function of temperature (°C). G', empty squares; G'', full squares, for each scaffold: (■) Col 24, (■) Col 48, (■) Col 72, and (■) Col 96

Table 2 Parameters obtained from the amplitude sweep measurements include the critical strain (γ_L), yield stress (τ_y), storage modulus at the LVE limit (G'_{LVE}), loss tangent (tan δ), crossover modulus (G'=G''), and the flow point stress (τ_f). Each parameter is defined once and the same notation is used consistently throughout the manuscript

Sample	γ_L (%)	τ_y (Pa)	G'_{LVE} (Pa)	tan δ	G'=G'' (Pa)	τ_f (Pa)
Col 24	4.69 ± 0.32^{ab}	15.80 ± 0.01^{a}	342.02 ± 22.86^{b}	0.19 ± 0.01^{c}	110.2 ± 3.39^{a}	91.76 ± 3.52^{c}
Col 48	5.36 ± 1.29^{a}	16.09 ± 3.68^{a}	304.43 ± 12.21^{b}	0.22 ± 0.01^{b}	83.76 ± 2.00^{b}	119.53 ± 3.13^{bc}
Col 72	3.23 ± 0.62^{b}	15.80 ± 0.01^{a}	497.10 ± 90.68^{a}	0.25 ± 0.01^{a}	84.68 ± 9.17^{b}	149.37 ± 13.30^{a}
Col 96	4.17 ± 0.73^{ab}	17.17 ± 2.37^{a}	417.63 ± 72.27^{ab}	0.23 ± 0.01^{b}	60.39 ± 4.64^{c}	128.93 ± 12.18^{ab}

Different lowercase letters on the same column show statistically significant differences by ANOVA and Tukey ($p \leq 0.05$)

Frequency sweep Figure 1B shows the curves of G' and G" over the studied frequency range (0.1–30 Hz). For all samples, G' remained higher than G" throughout the entire frequency range, indicating a predominantly elastic viscoelastic response typical of structured or concentrated polymer solutions. Moreover, both moduli were slightly dependent on frequency, increasing in higher frequency values. The increase in G' and G" moduli according to the increase in frequency was also observed for the calf skin collagen hydrogels obtained by Brazdaru et al. (2015).

According to the magnitude of G' and G", the logarithmic curves of both moduli as a function of frequency can be divided into three zones (Ferry 1989; Milan et al. 2022a): in the terminal zone, at low frequencies, the sample presents G">G', and its transition for the plateau zone only occurs after a crossover frequency. During most of the frequency range, G'>G" in the plateau zone, and the transition zone happens if a new crossover takes place. All the collagen solutions of this study were in the plateau zone (G'>G") in the entire frequency range, with no crossovers, which reflects their entanglements; probably, the number of entanglements in the collagen solutions, regardless of the hydrolysis time, was high enough to immobilize the polymeric structure into a network with fixed viscoelastic moduli (Lai et al. 2008).

G' and G" curves of Col 48 and Col 72 solutions, despite not presenting crossovers, had a different shape when compared to the other two solutions, in addition to much higher moduli values. For these samples, a rapid and sharp increase in the moduli was observed in the beginning of the assay, and then both moduli stabilized around 0.06 Hz. Such results indicate that the viscoelasticity of these solutions was more affected by small increases in frequency values in low frequency regions but quickly stabilized and became almost independent of the applied frequency in higher frequency regions.

Figure 1C shows the behavior of the complex dynamic viscosity (η*) of the collagen solutions according to the frequency. Determining the behavior of the collagen solutions viscosity (whether shear-thinning or thickening) when facing an applied frequency is important for their possible applications, and it is only feasible from a frequency sweep range (Diamantides et al. 2017). For all the samples, the dynamic viscosity decreased linearly with the increasing frequency, which is a typical non-Newtonian (shear-thinning) behavior (Razmkhah et al. 2017). Table 3 shows the values of η* for all the collagen solutions; the complex viscosity ranged from 58.45 ± 0.33 Pa s (Col 24) to 16,973 ± 3499 Pa s (Col 96), which is related to the higher elastic character of the collagen solutions that were subjected to longer hydrolysis time.

The slope of the dynamic viscosity curves (Table 3) also provides information about the viscoelastic structure of the solutions. When the slope approaches −1, the system exhibits reduced frequency dependence of its viscoelastic response, indicating a more structured and elastic behavior typically associated with highly entangled polymer solutions (Shatwell et al. 1991; Bertolo et al. 2023). The slopes of the collagen solutions went from −0.8424 ± 0.0263 (Col 24) to −0.9356 ± 0.0293 (Col 96), all with good adjustment of the data (R2 > 0.9986).

The slope close to −1 observed in the viscosity-frequency relationship may also raise the possibility of wall slip effects, which are commonly reported in rheological measurements of protein and biopolymer solutions. Wall slip occurs when a depletion layer forms near the measuring surface, reducing the apparent shear stress transmitted to the bulk material. In the present study, measurements were performed using a cone-plate geometry commonly employed for collagen systems. Although specific anti-slip geometries or gap-dependent tests were not performed, the consistency between steady shear, oscillatory measurements, and creep-recovery results suggests that the observed trends primarily reflect structural differences between the collagen solutions rather than experimental artifacts. Nevertheless, the potential influence of wall slip should be considered when interpreting the absolute viscosity values.

Table 3 Parameters determined from frequency sweep measurements for the collagen solutions obtained at different hydrolysis times: complex viscosity (η*, Pa s) at 1.0 Hz, the slope of η* and R^2 (obtained from the linear adjustment of η* curves from 0.03 to 30 Hz). Denaturation temperature (T_d) of the collagen solutions determined from the peak of tan δ curves in the temperature sweep measurements

Sample	η* (Pa s)	Slope η*	R^2	T_d (°C)
Col 24	58.45 ± 0.33^{b}	-0.8424 ± 0.0263^{b}	0.9990	42.07 ± 0.06^{a}
Col 48	57.62 ± 1.27^{b}	-0.8223 ± 0.0087^{b}	0.9992	41.03 ± 0.06^{b}
Col 72	$13{,}500 \pm 644^{a}$	-0.9256 ± 0.0272^{a}	0.9986	42.07 ± 0.40^{a}
Col 96	$16{,}973 \pm 3499^{a}$	-0.9356 ± 0.0293^{a}	0.9986	41.50 ± 0.46^{ab}

Different lowercase letters on the same column show statistically significant differences by ANOVA and Tukey ($p \leq 0.05$)

Temperature sweep Figure 1D shows the temperature dependence of the complex viscosity (η*), calculated from the viscoelastic moduli obtained during the temperature sweep measurements. In all cases, the viscosity decreased with increasing temperature, which is directly related to the higher energy of the collagen molecules at higher temperatures. The higher their energy, the weaker the resistance of the polypeptide chains to motion, which decreases the viscosity of the solutions. The decrease in the magnitudes of η* was more pronounced and sudden in the region from 35 to 40 °C, reflecting the collapse of the collagen triple helix

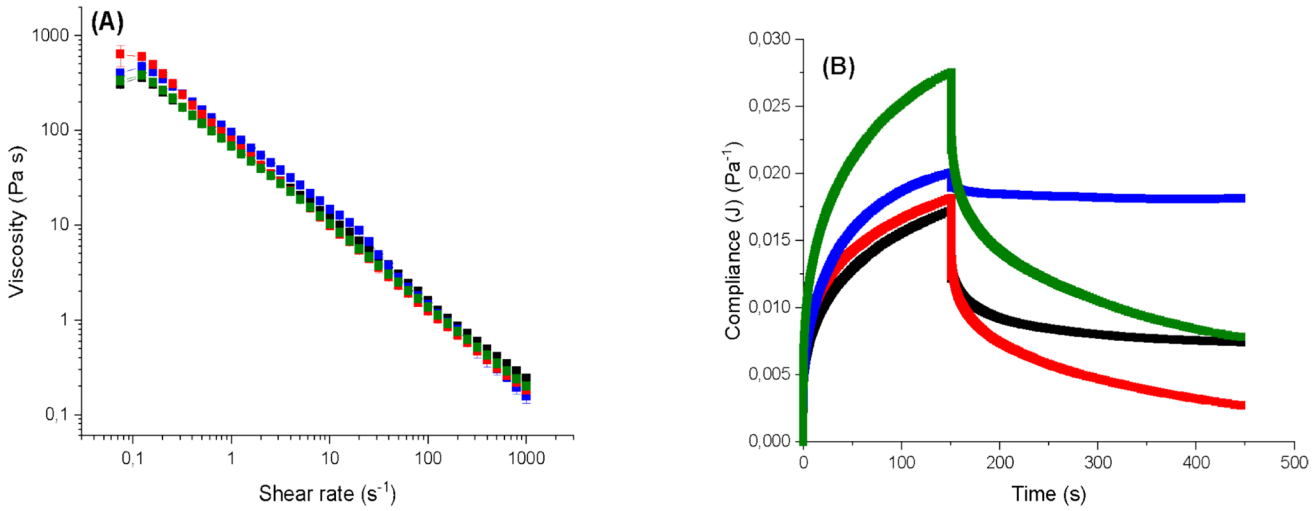

Fig. 2 **A** Viscosity (Pa s) as a function of shear rate (s^{-1}) in flow sweep and **B** Compliance (J(t), Pa^{-1}) as a function of time in creep-recovery measurements for: (■) Col 24, (■) Col 48, (■) Col 72, and (■) Col 96

Table 4 Parameters determined from the adjustment of flow curves to Cross model, from 0.1—1000 s^{-1}, for the collagen solutions obtained at different hydrolysis times: viscosity at zero shear (η_0, Pa s), consistency index (K, s), and rate index (n, dimensionless). Parameter determined from time-dependent measurements: % recovered compliance from creep-recovery curves

Sample	η_0 (Pa s)	K (s)	n	% Recovered compliance
Col 24	936.1 ± 88.64^{bc}	18.35 ± 4.65^{ab}	0.8475 ± 0.0147^{b}	45.81 ± 1.61^{a}
Col 48	688.23 ± 90.10^{c}	5.96 ± 1.31^{b}	0.9612 ± 0.0252^{a}	24.04 ± 10.65^{b}
Col 72	1818.67 ± 164.20^{a}	20.51 ± 7.37^{a}	0.9723 ± 0.0483^{a}	56.09 ± 2.90^{a}
Col 96	1153.00 ± 177.09^{b}	22.76 ± 3.97^{a}	0.8722 ± 0.0033^{b}	28.82 ± 5.38^{b}

Different lowercase letters on the same column show statistically significant differences by ANOVA and Tukey ($p \leq 0.05$)

structure to a random coil and, consequently, its denaturation (Zhang et al. 2010).

The denaturation temperatures (T_d) of the collagen solutions were determined as the temperatures where the increase of tan δ reached a peak value (Milan et al. 2022a) and are presented in Table 3. T_d values ranged from 42.07 ± 0.06 °C (Col 24) to 41.50 ± 0.46 °C (Col 96). The prolonged hydrolysis time seemed not to have affected collagen triple helix stability and did not decrease T_d values.

Steady shear tests

Figure 2A shows the curves of apparent viscosity as a function of shear rate for the collagen solutions obtained at different hydrolysis times. The shear-thinning behavior predicted by the frequency sweep measurements was confirmed, and all the solutions presented viscosities decreasing with the increase in shear rate.

At a same shear rate (0.1 s^{-1}), the apparent viscosities of the collagen solutions increased from 366.00 ± 39.96 Pa s (Col 24) to 469.13 ± 15.67 Pa s (Col 48) and 596.13 ± 17.45 Pa s (Col 72); for the solution with the longest hydrolysis time (Col 96), however, the apparent viscosity decreased to 380.43 ± 19.93 Pa s.

The curves were fitted using the Cross model (Eq. 1) to describe the shear-thinning flow behavior of the collagen solutions and to estimate empirical parameters such as the zero-shear viscosity (η_0), the consistency index (K), and the rate index (n). The model was used only as an empirical description of the steady-shear flow curves and does not imply a structural model of the collagen network. The curves were modeled from 0.1 to 1000 s^{-1}, and the parameters obtained are presented in Table 4.

η_0 is the magnitude of the viscosity of the solutions during storage, that is, pre shearing, and is related to the structure of the polymeric network, *i.e.*, to the loosening of the polymer aggregates, to eventual electrostatic repulsions that may be occurring between its molecules, and to the number of linkages between them (Razavi et al. 2016; Yang et al. 2018). η_0 values ranged from 936.1 ± 88.64 Pa s (Col 24) to 1153.00 ± 177.09 Pa s (Col 96).

The other parameters obtained from the Cross model are K (s), the consistency index, and n (dimensionless), the rate index (Table 4). The lower K, the more resistant against shear is the sample, and a greater Newtonian plateau is observed before the pseudoplastic behavior starts (Steffe, 1996; Bertolo et al. 2023). The samples with the greatest

K values were the ones obtained at the highest hydrolysis time, which indicates that prolonged hydrolysis led to solutions more sensitive to shear. Again, the greater net charge density of collagen in these solutions may be the explanation for this result: the higher number of carboxyl groups due to longer hydrolysis led to a charge repulsion between collagen molecules, reducing effective interactions between them. As a result, the shear-thinning effect was enhanced, and the solutions were more susceptible to flow (Yang et al. 2018).

Finally, the rate index of collagen solutions ranged from 0.8475 ± 0.0147 (Col 24) to 0.8722 ± 0.0033 (Col 96), which reinforces that all the solutions were pseudoplastic ($0 < n < 1$). As expected, K and n behaved in the opposite way (Yang et al. 2018): n increased from 24 to 48 h of extraction, indicating that Col 48 was a less pseudoplastic solution, but decreased again for the solutions with longer hydrolysis time (Col 72 and Col 96), confirming the tendency observed for K.

Creep-recovery tests

Figure 2B shows the curves of creep compliance J(t) as a function of time for the different collagen solutions; compliance is a direct indication of the softness of the sample, and the greater J(t), the weaker and more easily deformed is its internal structure (Yang et al. 2018). The % of recovered compliance (Table 4) could be calculated based on the recovery phase of the collagen solutions, acting as a direct result of the permanent deformation to which the solutions were subjected.

3D printability

Table 5 shows the printed samples (star and scaffold structures) based on anionic concentrated collagen solution (72 h). Col 72 resulted in printed samples without deformations, with $GF_{star\ angle}$: 104 ± 4%, $GF_{scaffold\ area}$: 98 ± 2% and EM: 84%.

Characterization of anionic collagen-based scaffolds

The denaturation temperature (T_d) of collagen (Fig. 3A and Table 6) was 47.87 °C for S_Col 24, 44.58 °C for S_Col 48, 43.24 °C for S_Col 72, and 42.64 °C for S_Col 96. FTIR-ATR spectra of all collagen scaffolds (Fig. 3B) showed a wide band centered at 3310 cm^{-1} that represents the combination of the axial deformation bands of OH and NH_3^+. The bands at 1633 and 1542 cm^{-1} correspond to the axial deformation of the C = O bond and the angular deformation of the N–H bond, respectively, which refer to the amide I and II bands. The spectra also presented characteristic bands in 1236 and 1448 cm^{-1} that can be attributed, respectively, to the amide III and the C-H bond of the pyrrolidine ring. The A_{1236}/A_{1448} bands ratio was near 1.0 for all collagen extracted from bovine tendon at different alkaline hydrolysis time (Table 6).

Figure 3B shows the FTIR spectrum of a native collagen from bovine tendon; the characteristic bands in the region of 3321 cm^{-1} referring to O–H and N–H deformations can also be seen for this collagen, as well as the bands at 1658 cm^{-1}

Table 5 Photographs, geometric fidelity (GF), and effective microporosity (EM) of 3D-printed star-shaped structures and scaffolds compared with their digital models

Shape	3D digital model	3D printed	Printability parameters
Star	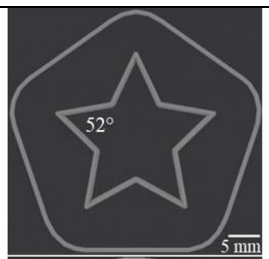	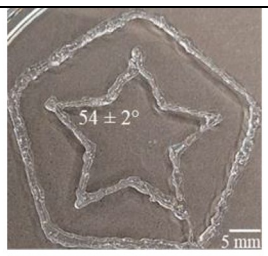	$GF_{star\ angle}$: 104 ± 4% $GF_{filament\ width}$: 103 ± 3%
Scaffold	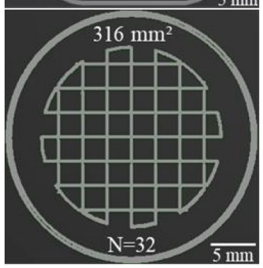	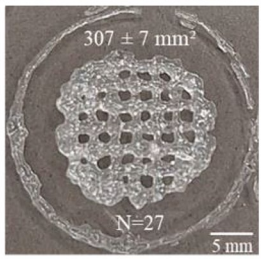	$GF_{scaffold\ area}$: 98 ± 2% EM: 84%

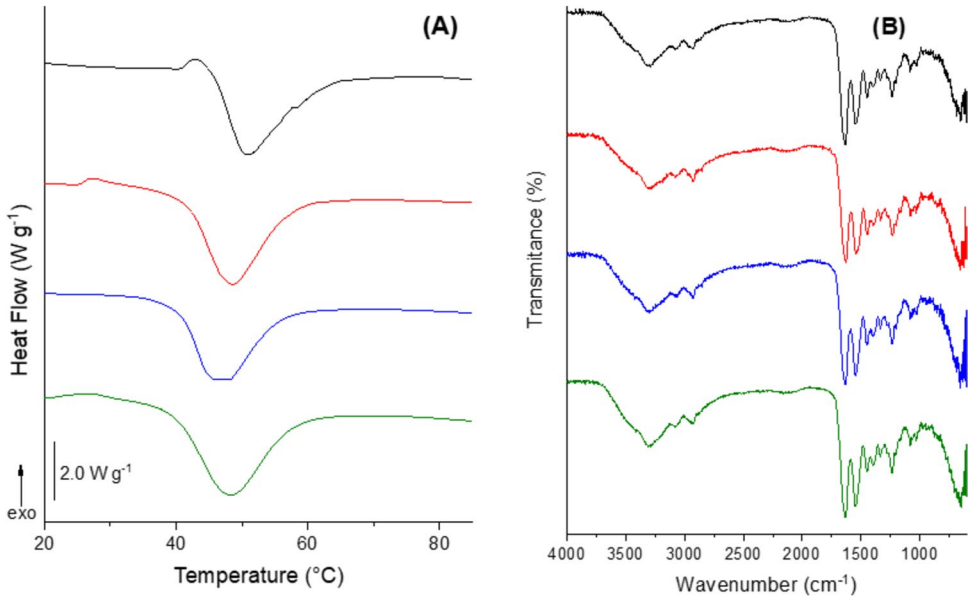

Fig. 3 **A** DSC curves and **(B)** ATR-FTIR spectra, for the scaffolds: (—) S_Col 24, (—) S_Col 48, (—) S_Col 72 and (—) S_Col 96

Table 6 Denaturation temperature (T_d) from DSC curves, A_{1236}/A_{1448} ratio from ATR/FTIR spectra, pore size from SEM images, porosity and % PBS absorption of the collagens obtained at different alkaline hydrolysis times

Sample	T_d (°C)	A_{1236}/A_{1448}	Pores size (μm)		Porosity (%)	PBS absorption (%) in 180 min
			Large	Small		
S_Col 24	47.87	0.99	108.9 ± 32.6[a]	11.3 ± 4.1[c]	99.3 ± 1.9[a]	3544 ± 224[b]
S_Col 48	44.58	1.01	95.1 ± 37.0[a]	42.3 ± 6.1[a]	94.2 ± 2.9[a]	3846 ± 449[b]
S_Col 72	43.24	0.99	63.8 ± 17.0[b]	16.9 ± 4.4[b]	101.4 ± 2.0[a]	4925 ± 199[a]
S_Col 96	42.64	1.02	61.0 ± 7.3[b]	12.2 ± 3.6[c]	93.9 ± 2.8[a]	5320 ± 240[a]

Different lowercase letters on the same column show statistically significant differences by ANOVA and Tukey ($p \leq 0.05$)

(characteristic of axial deformation of C = O and C-N bonds of amide I), at 1550 cm^{-1} (characteristic of angular deformations of N–H bonds of amide II), at 1450 cm^{-1} (referring to the pyrrolidine ring), and at 1236 cm^{-1} (characteristic of amide III). The A_{1236}/A_{1448} bands ratio was 1.01 for the native collagen, close to the ones calculated for the anionic collagens (Table 6). The assignment of the bands in the native collagen spectrum attests the complete removal of salts in the anionic collagens obtained at different times of alkaline hydrolysis, as well as the maintenance of the chemical stability of the collagens after such treatment, since no formation of new bands or change in the A_{1236}/A_{1448} ratio were observed.

The photomicrographs of the collagen (Fig. 4) showed that the alkaline hydrolysis time directly influenced the number of pores, which increased in longer hydrolysis. While S_Col 24 and S_Col 48 surfaces (Fig. 4A and B) showed pore formation with small open pores and large closed pores, S_Col 72 and S_Col 96 (Figs. 4C and D) had a greater number of large and small open pores. The interconnectivity of pores, which is also an important property for tissue regeneration, is exemplified in Fig. 4E for S_Col 72. Figure S2 shows the SEM photomicrograph of a scaffold of a native collagen from bovine tendon; as expected, the native structure is more similar to the structure of the anionic collagens obtained in shorter hydrolysis times (S_Col 24 and S_Col 48), *i.e.*, a more closed structure without interconnected pores.

Table 6 shows the size of the small (less than 50 μm in diameter) and large (greater than 50 μm in diameter) pores observed in the SEM images of the anionic collagen scaffolds. Hydrolysis time also had a great influence on the size of the pores, which decreased from 108.9 ± 32.6 μm (S_Col 24) to 61.0 ± 7.3 μm (S_Col 96). This tendency, however, was not observed for the small pores, and S_Col 48 stood out as the scaffold with significantly ($p \leq 0.05$) larger small pores (42.3 ± 6.1 μm), but fewer in number, when compared to the other scaffolds. Table 6 shows that the porosity values of the collagen scaffolds during various alkaline hydrolysis times were all consistently higher than 90%. Hydrolysis time did not significantly affect the porosity of the scaffolds, despite its attested influence on pore sizes.

The alkaline hydrolysis time led to a significant ($p \leq 0.05$) increase in PBS absorption capacity of the scaffolds from 3544% (S_Col 24) to 5320% (S_Col 96) in 180 min. Figure 5A shows the curves of PBS absorption as a function of time for all the scaffolds. The kinetic parameters for the PBS absorption of collagen scaffolds are shown in Table 7.

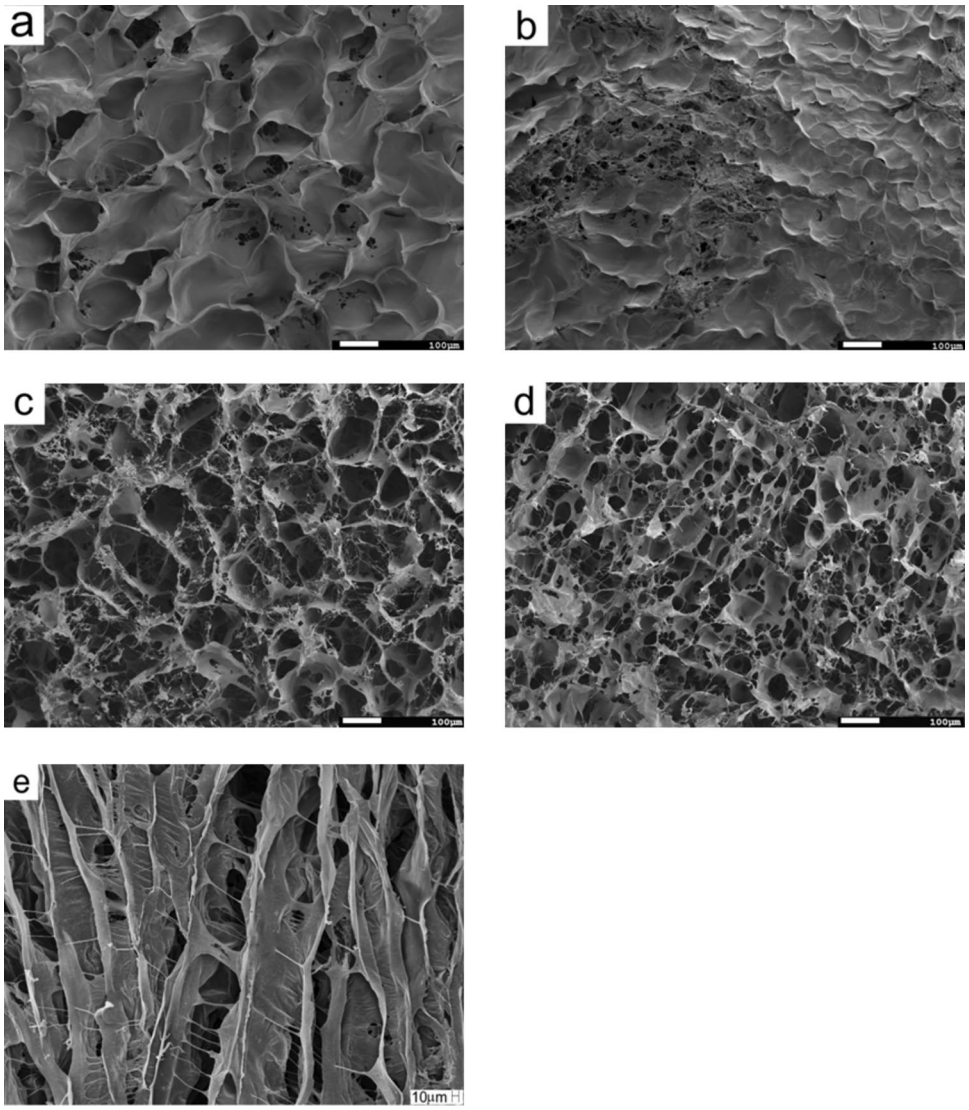

Fig. 4 SEM photomicrographs of the superficial section of: **a** S_Col 24, **b** S_Col 48, **c** S_Col 72 and **d** S_Col 96 scaffolds, with 100× magnification. **e** Transversal section of Col 72, with 500× magnification

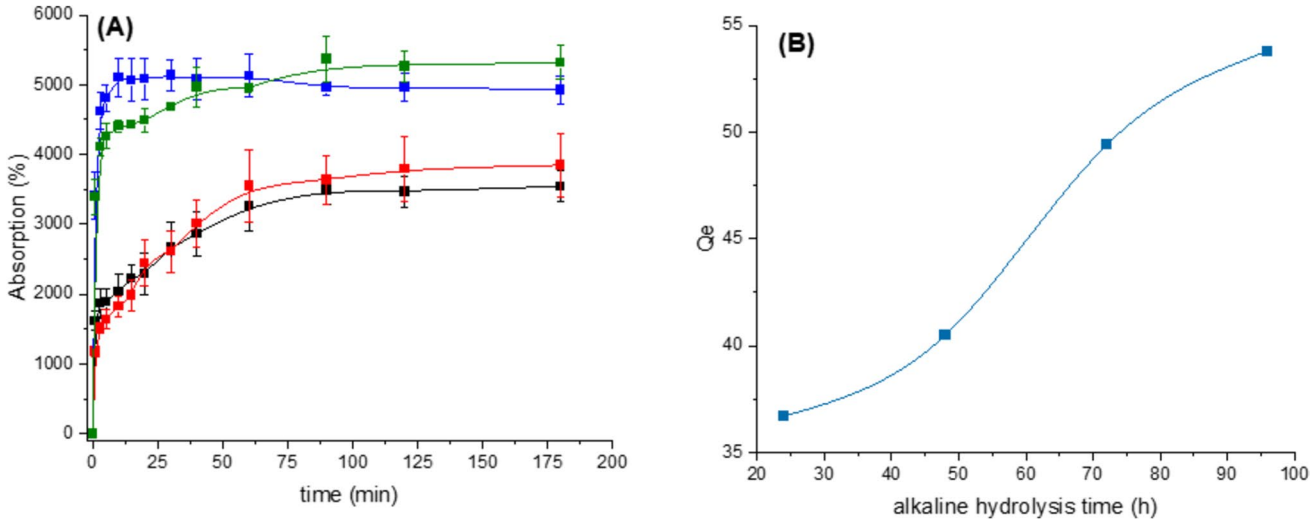

Fig. 5 **A** Curves of PBS absorption as a function of time for (–□–)S_Col 24, (—□—) S_Col 48, (—□—) S_Col 72 and (—□—) S_Col 96 scaffolds and **B** Swelling ratio in equilibrium (Q_e) as a function of alkaline hydrolysis time

Table 7 Kinetic parameters for the PBS absorption of collagen scaffolds

Sample	Order	k (min^{-1})	$Q_{e(observed)}$	$Q_{e(calculated)}$	R*
S_Col 24	*Pseudo 1*[a]	0.0333	35.5	20.9	0.9940
	Schott pseudo2[a]	**0.0038**		36.7	0.9981
S_Col 48	*Pseudo 1*[a]	0,0352	38.5	30.3	0.9926
	Schott pseudo2[a]	**0.0024**		40.5	0.9971
S_Col 72	*Pseudo 1*[a]	0.0084	51.3	6.1	0.7129
	Schott pseudo2[a]	**0.0440**		49.4	0.9999
S_Col 96	*Pseudo 1*[a]	0.0293	53.0	14.0	0.9819
	Schott pseudo2[a]	**0.0074**		53.8	0.9996

* Linear coefficient

In vitro assays

Figure 6A shows the percentage of cell viability for the scaffolds after 24 h of incubation. S_Col 24 showed 98.00% of viable cells, S_Col 48 101.01%, S_Col 72 94.58%, and S_Col 96 96.10%; S_Col 24 and S_Col 48 showed viability values significantly ($p \leq 0.05$) higher than the negative control, and all the samples presented viability values significantly higher than the positive control. Cell adhesion of Balbc-3T3 to the anionic collagen scaffolds was performed on 1 day, and the results are displayed in Fig. 6B. The samples presented attachment rates above 58% (58.74% for S_Col 24, 74.89% for S_Col 48, 74.10% for S_Col 72, and 73.55% for S_Col 96) (Fig. 6B).

Discussion

Characterization of anionic concentrated collagen solutions

Rheological measurements

Rheological measurements investigate the relationship between the structure of a polymeric material and its viscoelastic and flow properties (Brazdaru et al. 2015). Rheological responses allow predicting the processing of materials and modeling their properties and performance in the desired applications (Li et al. 2022). Thus, dynamic oscillatory, steady shear, and creep-recovery tests were conducted for bovine tendon collagen obtained at different alkaline hydrolysis time, aiming to relate how they may have influenced the collagen structure and, consequently, its rheological properties. The mechanical and viscoelastic properties of collagen solutions can be investigated as a function of deformation, frequency, temperature, and shear, simulating the most diverse experimental conditions to which the materials can be submitted during their application.

The rheological study of collagen solutions started with stress-controlled amplitude sweep measurements, which allow the determination of their viscoelastic properties as a function of the applied strain. From these measurements, two different regions can be determined: the first one is the so-called linear viscoelastic region (LVE), in which, regardless of the strain, G' (storage modulus) and G'' (loss modulus) remain constant (Fadavi et al. 2014). The LVE end

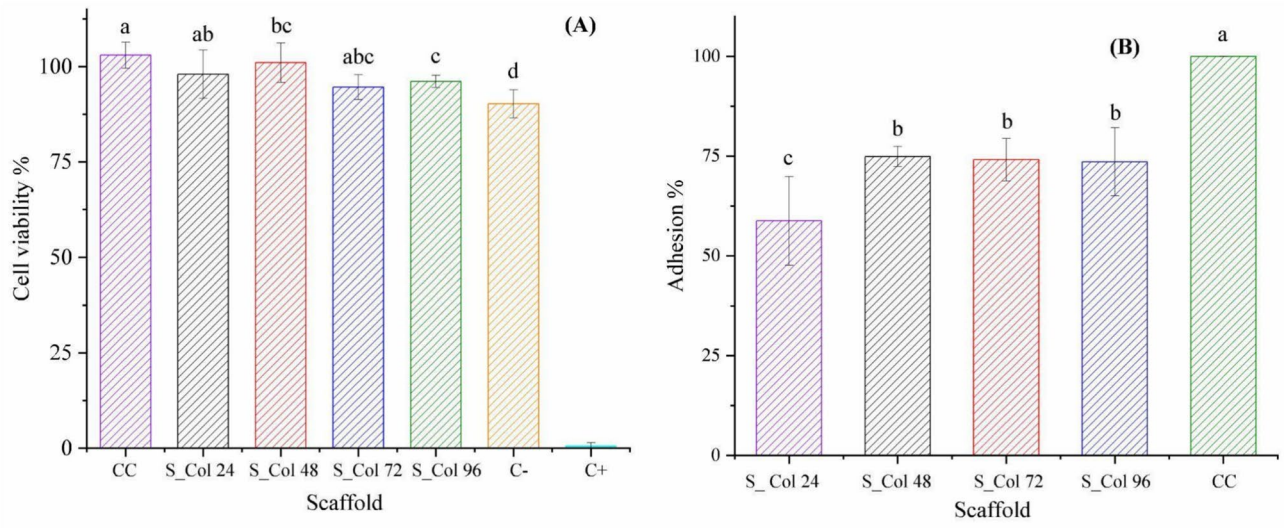

Fig. 6 **A** Percentage of Balbc-3T3 viability and **B** percentage of Balbc-3T3 adhesion to the anionic collagen scaffolds obtained at different hydrolysis times. Different lowercase letters on the same column show statistically significant differences by ANOVA and Tukey ($p \leq 0.05$)

marks the beginning of a region where both moduli start to decrease according to the increase in strain. From the parameters obtained with stress-controlled amplitude sweep measurements, it can be concluded that more rigid solutions (like Col 72 and Col 96) started to flow in higher flow point values but in lower moduli values, indicating that the disruption of the collagen network was faster for these samples.

Once LVE is determined by stress-controlled amplitude sweep measurements, frequency sweep assays performed at a fixed strain inside the LVE allow the classification of the solutions, according to the behavior of their viscoelastic moduli as a function of the frequency. All collagen solutions exhibited a predominantly elastic viscoelastic response, as indicated by the stress sweep results (G'>G" within the LVE). The parameters obtained from the frequency sweep measurements further indicated that increasing hydrolysis time led to more elastic and structured collagen solutions. Overall, the frequency sweep results are consistent with the stress sweep measurements regarding the influence of hydrolysis time on the viscoelastic properties of the collagen solutions.

The complex viscosity of the collagen solutions was also determined according to the temperature. During their processing, the solutions can be subjected to different temperatures, which may influence their viscosity and their behavior for the proposed application (Razmkhah et al. 2017). Understanding how the viscosity will behave in a determined temperature range can also bring some important information regarding these solutions, like the stability of their collagen triple helix and their denaturation process. The results from temperature sweep measurements indicated that the denaturation temperatures of the collagen solutions were not affected by hydrolysis time. These findings agree with the previous FTIR-ATR and DCS results and with what was reported by Bet et al. (2001), who analyzed the collagen stability according to the increase in the hydrolysis time by the ratio between the bands at 1235 and 1450 cm^{-1} in the infrared spectra and concluded that the triple helix was preserved in all the collagen solutions.

Steady shear measurements allow the prediction of the relationship between the shear rate applied to the sample and its internal structure, by analyzing the behavior of its apparent viscosity (Nik et al. 2005). The pseudoplastic behavior determined for the collagen solutions can be associated with molecular reorientation and partial disruption of physical intermolecular interactions with increasing shear; the molecules are then able to move past each other more easily, and the big aggregates give place to smaller ones, which are orientated towards the shear force, leading to the flow of the solutions, and decreasing their viscosities (Yang et al. 2018).

The increase in zero-shear viscosity according to hydrolysis time may be also attributed to the increase in negative charges in the polymeric network: collagen solubility increases due to the higher number of free carboxyl groups in the collagen molecules for the solutions obtained in longer hydrolysis. The higher the solubility of collagen in acetic acid during the extraction, the higher the viscosity of the solutions. Normah and Afiqah (2017) obtained similar results when comparing the viscosity of collagen extracted from skin croaker waste for 72 and 120 h, as a function of temperature. It is important to note that prolonged alkaline hydrolysis may also influence the molecular weight distribution of collagen molecules due to possible chain scission processes. In the present study, molecular weight characterization was not performed; therefore, direct conclusions regarding changes in molecular size cannot be drawn. Consequently, the rheological variations observed here are interpreted primarily in terms of changes in charge density and intermolecular interactions, although potential molecular weight effects cannot be excluded.

Creep and recovery measurements were conducted in order to analyze further changes in the internal structure of the collagen solutions as a function of the applied stress during a period of time. For that, a constant stress (10 Pa) was applied to all the solutions in a time interval of 0–150 s and, when the stress was removed, the recovery of the sample's deformation was measured from 150 to 450 s.

Creep and recovery measurements revealed differences in the deformation and recovery behavior of the collagen solutions as a function of hydrolysis time. During the creep step, samples obtained at longer hydrolysis times exhibited higher compliance, indicating increased susceptibility to deformation under constant stress, which can be attributed to enhanced electrostatic repulsion between collagen molecules and partial loosening of the physically entangled network.

The recovery behavior, however, did not follow a monotonic trend with hydrolysis time. Col 72 exhibited the highest recovered compliance (56.09±2.90%), indicating a more effective partial structural recovery after stress removal when compared to the other samples. This suggests that an intermediate hydrolysis time promoted a favorable balance between network connectivity and molecular mobility, enabling greater elastic recovery. In contrast, the lower recovery observed for Col 96 indicates that excessive charge density hindered network reorganization, leading to increased permanent deformation. Overall, the incomplete recovery observed for all samples reflects the viscoelastic nature of physically structured collagen networks (Yang et al. 2018).

The mechanical and viscoelastic behavior observed for the anionic collagen solutions is consistent with previously reported collagen-based bioink systems. Storage) values in the range of hundreds of pascals, as observed for the

samples in this study (300–500 Pa), are typical of physically structured collagen systems prior to crosslinking. Similar magnitudes have been reported for collagen solutions and collagen-based bioinks intended for extrusion printing, where G' values commonly range from tens to several hundred pascals depending on concentration and modification strategy (Diamantides et al. 2017; Milan et al. 2022a).

Compared with chemically crosslinked collagen systems, the present materials exhibit lower elastic moduli, which is expected since no additional crosslinking agents were used. modulus (G'.

Crosslinked collagen hydrogels or collagen composites reinforced with nanoparticles or secondary polymers frequently reach storage moduli in the kilopascal range, reflecting the formation of more permanent network junctions. Nevertheless, lower-modulus collagen systems such as the ones presented here can be advantageous during extrusion-based printing, as moderate viscoelastic strength combined with shear-thinning behavior facilitates flow through the nozzle while still enabling partial shape retention after deposition.

In comparison with commercial bioinks or composite collagen systems, which often incorporate polymers such as alginate, gelatin methacrylate, or synthetic components to enhance mechanical stability, the anionic collagen solutions evaluated in this work represent a simpler single-component system. Despite the absence of reinforcing phases or chemical crosslinking, the Col 72 formulation exhibited rheological characteristics suitable for extrusion printing, including a dominant elastic response (G'>G"), shear-thinning behavior, and partial structural recovery. These results indicate that tuning the charge density through alkaline hydrolysis provides a viable strategy to modulate collagen network organization and obtain rheological properties within the range required for biofabrication processes. Therefore, based on the rheological results, Col 72 was selected as the test sample for printability assays and used as a representative case study within the proposed framework.

3D printability

Col 72 produced printed structures with less smooth, thicker filaments and lower definition compared to the 3D digital model (Table 5). This behavior may be attributed to the rheological properties of the ink, which exhibited a predominantly elastic response within the linear viscoelastic region (G'>G"), a key requirement for shape retention in extrusion-based printing, but with tan δ values characteristic of concentrated polymer solutions rather than true gels. According to the literature, bioinks with intermediate tan δ values may flow readily under shear but exhibit limited structural rebuilding after deposition, favoring filament spreading (Montalbano et al. 2023). In addition, Col 72 displayed pronounced shear-thinning behavior, which is advantageous for extrusion through the nozzle but may compromise dimensional accuracy when elastic recovery is not sufficiently fast. Creep–recovery results further support this interpretation, as the partial recovered compliance indicates slow and incomplete structural reorganization after stress removal, suggesting limited thixotropic rebuilding. Consequently, although Col 72 presented high structural strength, the combination of moderate elastic recovery and pseudoplastic flow was not sufficient to fully support multilayer stacking, resulting in filament thickening and reduced definition.

Despite this, the global and local geometric fidelity of both the star-shaped structure and the scaffold was considerably high (Table 5), with printed structures similar to the 3D digital models, allowing the distinction of the star angles and the scaffold macropores. The geometric fidelity of the star-shaped structure was higher than 100%, indicating that the angles formed in the printed star were larger than those of the digital model. The filament width was 1.23 ± 0.11 mm, closely matching the needle diameter (1.22 mm) and exhibiting a low coefficient of variation (~9%), which confirms good printing reproducibility. Similar to the star angles, the filament width also exhibited geometric fidelity values above 100%. This behavior may be attributed to rounding or expansion at the star extremities as a consequence of the viscoelastic nature of the Col 72 ink, particularly its limited elastic recovery after extrusion and the balance between elastic and viscous contributions ($\tan \delta < 1$), which promotes filament relaxation at regions of higher curvature (Montalbano et al. 2023; Yang et al. 2018).

For the scaffold, area-based geometric fidelity was high, ensuring shape reproducibility and control of the printing process. The effective macroporosity of the scaffold, however, was lower due to the merging of some lines deposited during printing, which can be attributed to insufficient layer self-support associated with the viscoelastic behavior of the ink and its limited post-deposition recovery. Similar effects have been reported for collagen-based and other biopolymer inks exhibiting pseudoplastic flow and incomplete post-deposition recovery, leading to filament spreading and reduced pore definition (Montalbano et al. 2023; Sponchiado et al. 2024). Despite this, the area-based geometric fidelity of the scaffold was higher than that reported for scaffolds produced with thermally modified potato starch, while the effective macroporosity was similar (Sponchiado et al. 2024). These results indicate the potential of Col 72 as an ink for 3D printing of biomaterials, for example, considering that starch-based inks have been widely reported as among the most promising systems for this application (Joseph et al. 2024; Koski and Bose 2019).

In addition to rheological behavior, the optimization of printing parameters, ink formulation, and the application of post-printing treatments can substantially improve the quality of printed structures. Biomimetic scaffolds with high geometric fidelity have been successfully printed using type I collagen–based inks reinforced with nanohydroxyapatite and bioglass nanoparticles (Montalbano et al. 2023). The produced inks exhibited pseudoplastic behavior and rapid shear recovery, which was ensured by post-printing crosslinking with genipin. Furthermore, the formation of blends between collagen and other biopolymers, such as chitosan (Jirofti et al. 2023) or poly(ε-caprolactone) (Pei et al. 2023), may represent an effective strategy to enhance printability and reproducibility of the printed structures.

Overall, the results indicate that Col 72 is a promising ink for 3D printing of biomaterials, enabling the fabrication of scaffolds with adequate geometric fidelity. Further studies focusing on formulation optimization and process parameters are required to improve printability and expand its potential applications.

Characterization of anionic collagen-based scaffolds

The denaturation temperature (T_d) of collagen, *i.e.*, the temperature at which the disruption of its interactions leads to the disorganization of the collagen matrix, was determined by DSC. T_d serves as an indicator of stability, with higher values suggesting greater stability. This increased stability is often attributed to stronger inter-chain bonds resulting from bond formation, reduction in internal water content, or other factors (Trębacz et al. 2018). The results (Fig. 3A) show that the integrity of the secondary structure of the triple helix was preserved at all hydrolysis times evaluated. The S_Col 96 exhibited a Td of 42.64 °C, consistent with previously reported values for collagen extracted (Milan et al. 2022b). Additionally, the T_d values of the collagenic scaffolds show a decreasing trend as a function of hydrolysis time (Table 6). The disruption of crosslinks in the tissue and changes in the formation of microfibrils are leading to an increase in negative charges in the collagen scaffold and to a new pattern of electrostatic interactions, which directly affects collagen thermal stability. This increase in negative charges occurs due to the hydrolysis of amino groups of asparagines and glutamines residues, which are present in the tropocollagen chain, leading to a value 1.3 times higher (Bet et al. 2001).

FTIR-ATR spectra of all collagen scaffolds presented characteristic bands related to the integrity of the triple helix structure of collagen in 1236 and 1448 cm^{-1}. While the first band is sensitive to the presence of secondary structure, the second band is independent of the ordered structure of tropocollagen. When the ratio of absorbances in 1236 and 1448 cm^{-1} is greater or equal to the unit, the triple helix structure is preserved, while for the denatured structure this ratio is found around 0.5 (Milan et al. 2021). The A_{1236}/A_{1448} bands ratio was near 1.0 for all collagen extracted from bovine tendon at different alkaline hydrolysis time, as well as for a native collagen from bovine tendon, which confirms the integrity of the triple helix of collagen that had been pointed out by DSC results. Ju et al. (2020) analyzed by FTIR-ATR the triple helix integrity of native collagen fibrils derived from bovine tendons using acid-solubilized and pepsin-assisted extraction; the authors reported that although the ratio of A_{1236}/A_{1448} bands was 0.99 for both collagens, the secondary structure of the collagen extracted with the acid-solubilized method was more prominent and complete, due to the intensity of the Amide II and Amide III bands that were critically distinguished from the intensity of the absorption peaks (Ju et al. 2020). Such distinction, however, could not be observed in the spectra of collagens obtained at different hydrolysis times in this study, which supports the hypothesis that the chemical structure of collagen was preserved.

The design of scaffolds has a direct impact on their use as biomaterials and the presence and size of pores can dictate the best application for these materials. Furthermore, the suitable pore size depends on the type of cell used: pores smaller than 20 µm, for instance, are required for chondrogenic growth, whereas pores larger than 80 µm are promising for fibrogenic ingrowth (Sun et al. 2018; Zhang et al. 2022). Scaffolds must be porous to facilitate the diffusion of nutrients, oxygen, and waste materials. Likewise, pores and their interconnectivity are used for cell nutrition, proliferation, and migration, as well as for tissue vascularization and formation of new tissues. Several studies show that pores > 300 µm provide space for bone growth and vascularization, and pores < 20 µm favor the capillarity of the bone scaffold, which leading to the increase the number and variety of cells. More specifically, the ideal range for fibroblast growth is from 20 to 120 µm (Song et al. 2018; Yadav et al. 2021).

In tissue regeneration, different descriptions of pore sizes have been postulated. Among them, macropores are defined as pores > 50 µm, while micropores are defined as pores < 50 µm or < 10 µm (Perez and Mestres 2016). Pore sizes are also defined as macro (> 100 µm), micro (100 nm – 100 µm), and nano (< 100 nm) (Vagaská et al. 2010), or even nano (< 100 nm), submicron (100 nm – 1 µm), micron (1–100 µm), and macro (> 100 µm) (Ebrahimi 2021). The scaffolds developed in this study were categorized as having large and small pores, due to their high number of pores of different sizes. The alkaline hydrolysis time directly influenced the number of pores, which increased in longer hydrolysis, and also had a great influence on the size of the pores, as observed in this study.

Kaczmarek-Szczepańska et al. (2023) studied the morphology of collagen-based scaffolds modified with three different phenolic acids. The collagen scaffolds had pore diameters of 112 ± 14.2 µm, and the inclusion of caffeic, ferulic, and gallic acids led to diameters of 108 ± 21.1, 162 ± 17.8, and 115 ± 25.6 µm, respectively. The authors concluded that the different treatments did not modify the morphology of collagen scaffolds, different from what was observed in this study regarding hydrolysis time. Putri et. al. (2020) presented collagen scaffolds prepared by dissolving porcine type I collagen in a mixture solution of ethanol and acetic acid and by adding free ice particulates; the resultant structure presented pores size of 114 ± 27 µm.

Several other studies about collagen obtained by alkaline hydrolysis showed pore sizes consistent with those described here. Milan et al. (2022b) used alkaline hydrolysis for 96 h in bovine tendon and showed scaffolds with pore sizes of 46.4 ± 3.5 µm. In Milan et al. (2021), an alkaline hydrolysis for 48 h in fish skin provided scaffolds with pore sizes of 85.0 ± 7.4 µm. Garcia et al. (2021), in turn, obtained scaffolds with pores of 58.7 ± 28.7 µm by treating bovine serosa with an alkaline hydrolysis for 120 h. Horn and Martins (2009) obtained scaffolds from porcine serosa and also varied the time of alkaline hydrolysis, showing pores size such as 163.9 ± 12.4 µm (24 h) and 67.1 ± 4.7 µm (72 h); the authors observed the same tendency of decreasing pore size with increasing hydrolysis time, as observed in this study.

Porosity is a relevant factor when it comes to tissue regeneration because the nature of the nutrient flow is determined by size, geometry, interconnectivity, direction, and surface chemistry of the scaffold channels. Scaffolds with good connectivity assist in fluid transport into the biomaterial and the interconnection of channels allows cell migration (Zhang et al. 2022). Zhao et al. (2019) stated that the suitable porosity for a scaffold for bone growth is between 60 and 95%. Moreover, the early attachment, diffusion, and proliferation of fibroblasts occur in both low- and high-porosity scaffolds (60–90%), but the migration and infiltration of active cells is supported only in high-porosity scaffolds (Zhao et al. 2019). Masson-Meyers et al. (2023) developed collagen scaffolds with average diameter of pores of 435 µm and high porosity (85%). Despite the high porosity, the scaffolds developed in this study were still more porous, with an adequate morphology for possible application in tissue regeneration.

The ability of scaffolds to absorb liquid is a crucial property to assess their effectiveness for tissue regeneration, since it is directly related to an adequate nutrient supply for cell adhesion and proliferation (Grover et al. 2012; Wang et al. 2023).

The increase in PBS absorption capacity of the scaffolds can be primarily attributed to the increase in collagen hydrophilicity, which is a consequence of the higher number of negative charges in the collagen structure (Bet et al. 2001). S_Col 24 and S_Col 48 absorbed less and exhibited similar absorption patterns, which may also be attributed to their similar morphologies, characterized by large and non-open surface pores. The same explanation applies to S_Col 72 and S_Col 96, which have open pores on their surfaces, thus favoring liquid absorption.

Garcia et al. (2021) obtained scaffolds of anionic collagen combined with plant extracts, with the scaffold containing jabuticaba extract showing a maximum absorption at 3057.1%, while the pure collagen sample exhibited a value of 1337.2%. Massimino et al. (2020) suggested that pore size directly influences this property, as the addition of auricular cartilage to anionic collagen scaffolds resulted in matrices with smaller pore sizes and lower absorption capacity. These findings are consistent with the results obtained in this study, indicating that the scaffold morphology directly influences its absorption capacity. Therefore, collagen-based scaffolds could be of great interest for use in tissue regeneration applications, given their ability to modulate absorption properties according to morphological characteristics.

The absorption rate of PBS in the scaffolds was examined by analyzing experimental swelling data using kinetic models of pseudo-first order and pseudo-second order (Ghosh et al. 2018; Moshayedi et al. 2021; Matar et al. 2022). The pseudo-first order kinetic model is expressed by Eq. (9):

$$ln\,(Q_e - Q_t) = lnQ_e - k_1 t \tag{9}$$

In the equation, *Qe* and *Qt* are the values of the mass of PBS absorbed per unit mass ($mg.mg^{-1}$) at equilibrium and time *t*, respectively and k_1 (min^{-1}) is the pseudo-first-order adsorption rate constant (Vargas-Rodríguez et al. 2021). Thus, through the linear regression of the graph of ln*(Qe-Qt)* vs time the values of inclination ($-k_1$) and intercept (ln *Qe*) were obtained.

Equation (10) describes the kinetic model of pseudo-second order or Schott model:

$$\frac{t}{Q_t} = \frac{1}{k_2 Q_e^2} + \left(\frac{1}{Q_e}\right) \times \; t \tag{10}$$

In the equation, Q_e is the ratio of swelling in equilibrium, Q_t is the ratio of swelling in time *t*, both in $mg.mg^{-1}$, and k_2 is the rate constant for swelling (min^{-1}) in pseudo-second order (Tang et al. 2012).

In this model, *t/Qt* was plotted as a function of *t* and the line (1/*Qe*) and the intercept ($1/((k_2\,Qe^2))$) and thus k_2 were obtained through linear regression.

The kinetic swelling parameters obtained for the collagen scaffolds shown in Table 7 indicate that the Schott model

was the best fit for all the samples (Moshayedi et al. 2021). The *Qe* values calculated by the Schott model are in accordance with the experimental observations and increase as alkaline hydrolysis time increases (Fig. 5B). The absorption was about 1.5 times greater in 96 h of alkaline hydrolysis than in 24 h, which can be justified by the increase in the content of negative charges that occurs in longer hydrolysis, as explained previously in DSC results (Bet et al. 2001).

Although Fig. 5B suggests a tendency toward a plateau in the equilibrium swelling ratio with increasing hydrolysis time, longer alkaline hydrolysis durations were not explored in this study. Prolonged hydrolysis is known to progressively increase the density of negatively charged groups in collagen while simultaneously promoting disruption of intermolecular crosslinks and partial degradation of the molecular structure. Excessive hydrolysis may therefore compromise the structural integrity and functional properties of the collagen matrix. For this reason, the range of hydrolysis times investigated (24–96 h) was selected to balance the increase in charge density with the preservation of the collagen structure.

In vitro assays

A biomaterial intended to be used in tissue regeneration must not only have appropriate morphological characteristics, but also be biocompatible. Collagen is widely used as a biomaterial for tissue regeneration due to its biocompatibility (Wang et al. 2023), and is expected not to present cytotoxicity. Therefore, the cytotoxicity assay was performed to confirm the effects of the different hydrolysis times for the extraction of anionic collagen in this study.

Cell viability is inversely proportional to cytotoxicity, that is, the higher the cell viability, the lower the cytotoxicity of the tested material. Therefore, biomaterials with cellular viability lower than 30% are considered as having an intense degree of cytotoxicity; from 30 to 60%, the cytotoxicity degree is moderate, while from 60 to 90% is light; finally, cell viability above 90% represents noncytotoxic materials (Lönroth and Dahl 2003; Sukumaran et al. 2023).

Yang et al. (2023) demonstrated that their collagen-based bilayer membranes modified with dialdehyde carboxymethyl cellulose + dehydrothermal treatment exhibited cytocompatibility above 100%. Nocera et al. (2018) developed a 3D printed collagen scaffold with viability of 85.07 ± 6.73%. Likewise, none of the scaffolds obtained in this study showed toxic effects according to ISO 10993–5 (2009), which recommends cell viability greater than 70%. Therefore, the alkaline hydrolysis time did not interfere with the biocompatibility of the materials and these results are promising for the continuation of the study.

Cell adhesion, migration, and proliferation are directly affected by the morphology of the scaffolds. According to Yang et al. (2023), cell migration is restricted when the pores are too small, impairing nutrient diffusion and waste elimination. Otherwise, larger pores suppress cell adhesion because of the decrease of adhesion surface area. Therefore, developing scaffolds with a balance between the most favorable pore size and surface area for cell adhesion has an important role in promoting tissue regeneration.

The samples presented attachment rates between 58.74% for S_Col 24 and 74.89% for S_Col 48. This variation in cell adhesion rate may be related to the morphology of the scaffolds. S_Col 24 did not have many open surface pores, which made the cell adhesion process difficult and led to a significantly ($p \leq 0.05$) lower value of adhesion for this sample (ISO 10,993–5, 2009; Zhang et al. 2022).

Yang et al. (2023) developed collagen membranes that can support the ingrowth of fibroblasts and osteoblasts. McGarry et al. (2023) compared natural and synthetic polymers scaffolds and concluded that synthetic PLA scaffold facilitated cellular attachment, but did not promote cell migration and proliferation, in contrast with the natural collagen scaffold. Therefore, it was proved that the hydrolysis used to obtain anionic collagen in this study was promising, since the scaffolds showed favorable cell adhesion.

Taken together, these results indicate that hydrolysis time governs a transition from a highly connected but mechanically rigid collagen network to a charge-dominated system with enhanced flowability but reduced structural recovery, thereby defining a narrow processing window for biofabrication. This study is intentionally focused on establishing rheological–structural relationships and early cytocompatibility as a first design step. Comprehensive mechanical testing of printed constructs and advanced biological assays, including differentiation and functional outcomes, will be addressed in future studies to extend the translational relevance of this framework.

Conclusion

Different alkaline hydrolysis times were employed to obtain anionic collagen solutions. A rearrangement of the three-dimensional collagen network towards more elastic solutions with longer hydrolysis was attested by rheological assays. The zero-shear viscosity of collagen solutions increased according to hydrolysis time, which points to the increase in negative charges in the polymeric network in longer treatments. Col 72 was used as a proof of concept for scaffold ink production, demonstrating that anionic collagen can be employed in the development of biomaterial inks. All scaffolds obtained from these solutions presented triple helix integrity with denaturation temperature values decreasing with increasing hydrolysis time. The number

of open pores was higher for the scaffolds obtained with longer hydrolysis, but the opposite effect was observed for their size, which decreased. Hydrolysis time did not significantly affect the porosity of the scaffolds but increased their absorption capacity due to the formation of more negative charges and the increase in the hydrophilicity of collagen. All the scaffolds prepared showed high cell viability and adhesion values, despite the treatment time, suggesting that they can be utilized in the regeneration of various types of tissues. Overall, this work demonstrates that alkaline hydrolysis time can be used as a tunable design parameter to engineer anionic collagen bioinks, offering a predictive, rheology-based framework to guide formulation selection and printability in extrusion-based biofabrication. Future studies should focus on mechanical reinforcement strategies, long-term biological assessments, and further optimization of processing and printing parameters to enhance structural stability, functionality, and translational potential. These efforts will be essential to expand the applicability of anionic collagen-based systems in more complex and clinically relevant tissue engineering scenarios.

Supplementary Information The online version contains supplementary material available at https://doi.org/10.1007/s00397-026-01567-6.

Acknowledgements This study was financed in part by the following Brazilian institutions: Coordenação de Aperfeiçoamento de Pessoal de Nível Superior—Brasil (CAPES)—Finance Code 001. Conselho Nacional de Desenvolvimento Científico e Tecnológico—Brasil (CNPQ) – Process number: 382268/2020-2; 153726/2024-5; 157788/2025-3; 303423/2025-0.
São Paulo Research Foundation (FAPESP)—Process number: 2020/08727-0; 2024/02072-3; 2024/10994-8.
We thank the Multipurpose Gamma Irradiation Facility – CETER/IPEN for sterilizing the samples.

Author contribution The manuscript was written through contributions of all authors. All authors have given approval to the final version of the manuscript.

Funding The Article Processing Charge (APC) for the publication of this research was funded by the Coordenação de Aperfeiçoamento de Pessoal de Nível Superior - Brasil (CAPES) (ROR identifier: 00x0ma614).

Declarations

Conflict of interest The authors declare that they have no conflict of interest.

Competing interest The authors declare that they have no known competing financial interests or personal relationships that could have appeared to influence the work reported in this paper.

References

Amirrah IN, Lokanathan Y, Zulkiflee I, Wee MFMR, Motta A, Fauzi MB (2022) A comprehensive review on collagen type I development of biomaterials for tissue engineering: from biosynthesis to bioscaffold. Biomedicines 10:2307. https://doi.org/10.3390/biomedicines10092307

Bazrafshan Z, Stylios GK (2019) Spinnability of collagen as a biomimetic material: a review. Int J Biol Macromol 129:693–705. https://doi.org/10.1016/j.ijbiomac.2019.02.024

Bertolo MRV, Martins VCA, Plepis AMG, Bogusz Junior S (2023) Acerola (*Malpighiaemarginata*) and açaí (*Euterpeoleracea*) extracts as active compounds of starch/gelatin-based solutions: rheological characterization. Colloids Surf A Physicochem Eng Asp 676:132288. https://doi.org/10.1016/j.colsurfa.2023.132288

Bet MR, Goissis G, Lacerda CA (2001) Characterization of polyanionic collagen prepared by selective hydrolysis of asparagine and glutamine carboxyamide side chains. Biomacromol 2:1074–1079. https://doi.org/10.1021/bm0001188

Brazdaru L, Micutz M, Staicu T, Albu M, Sulea O, Leca M (2015) Structural and rheological properties of collagen hydrogels containing tannic acid and chlorhexidine digluconate intended for topical applications. CR Chim 18:160–169. https://doi.org/10.1016/j.crci.2014.07.007

Diamantides D, Wang L, Pruiksma T, Siemiatkoski J, Dugopolski C, Shortkroff S, Kennedy S, Bonassa LJ (2017) Correlating rheological properties and printability of collagen bioinks: the effects of riboflavin photocrosslinking and pH. Biofabrication 9:034102. https://doi.org/10.1088/1758-5090/aa780f

Djabourov M, Lechaire JP, Gaill F (1993) Structure and rheology of gelatin and collagen gels. Biorheology 30:191–205. https://doi.org/10.3233/bir-1993-303-405

Ebrahimi M (2021) Porosity parameters in biomaterial science: definition, impact, and challenges in tissue engineering. Front Mater Sci 15(3):352–373. https://doi.org/10.1007/s11706-021-0558-4

Fadavi G, Mohammadifar MA, Zargarran A, Mortazavian AM, Komeili R (2014) Composition and physicochemical properties of Zedo gum exudates from *Amygdalus scoparia*. Carbohydr Polym 101:1074–1080. https://doi.org/10.1016/j.carbpol.2013.09.095

Fan L, Ren Y, Emmert S, Vučković I, Stojanovic S, Najman S, Schnettler R, Barbeck M, Schenke-Layland K, Xiong X (2023) The use of collagen-based materials in bone tissue engineering. Int J Mol Sci 24:3744. https://doi.org/10.3390/ijms24043744

Ferry JD (1989) Viscoelastic properties of polymers. Wiley, New York, p 369

Figueiredo MP, Rodríguez-Fernández S, Copes F, Mantovani D (2025) Review of collagen type I-based hydrogels: focus on compositionstructure-properties relationships. NPJ BioMed Innov 2:16. https://doi.org/10.1038/s44385-025-00018-w

Garcia CF, Marangon CA, Massimino LC, Klingbeil MFG, Martins VCA, Plepis AMG (2021) Development of collagen/nanohydroxyapatite scaffolds containing plant extract intended for bone

regeneration. Mater Sci Eng C Mater Biol Appl 123:111955. https://doi.org/10.1016/j.msec.2021.111955
Gautieri A, Vesentini S, Redaelli A, Buehler MJ (2011) Hierarchical structure and nanomechanics of collagen microfibrils from the atomistic scale up. Nano Lett 11:757–766. https://doi.org/10.1021/nl103943u
Ghosh SK, Das A, Basu A, Halder A, Das S, Basu S, Abdullah MF, Mukherjee A, Kundu S (2018) Semi-interpenetrating hydrogels from carboxymethyl guar gum and gelatin for ciprofloxacin sustained release. Int J Biol Macromol 120:1823–1833. https://doi.org/10.1016/j.ijbiomac.2018.09.212
Grover CN, Cameron RE, Best SM (2012) Investigating the morphological, mechanical and degradation properties of scaffolds comprising collagen, gelatin and elastin for use in soft tissue engineering. J Mech Behav Biomed Mater 10:62–74. https://doi.org/10.1016/j.jmbbm.2012.02.028
Horn MM, Martins, VCA, Plepis, AMG (2009) Interaction of anionic collagen with chitosan: effect on thermal and morphological characteristics. Carbohydr Polym 77:239–243. https://doi.org/10.1016/j.carbpol.2008.12.039
International Organization for Standardization (2009) ISO 10,993–5: biological evaluation of medical devices - part 5: tests for in vitro cytotoxicity. Genebra
International Organization for Standardization (2012) ISO 10,993–12: Biological evaluation of medical devices - Part 12: Sample preparation and reference materials. Genebra
International Organization for Standardization (2017) ISO 11,137–3: Sterilization of health care products - Radiation - Part 3: Guidance on dosimetric aspects of development, validation and routine control. Genebra
Jirofti N, Hashemi M, Moradi A, Kalalinia F (2023) Fabrication and characterization of 3D printing biocompatible crocin-loaded chitosan/collagen/hydroxyapatite-based scaffolds for bone tissue engineering applications. Int J Biol Macromol 252:126279. https://doi.org/10.1016/j.ijbiomac.2023.126279
Joseph A, Muhammad LFS, Vijayan A, Xavier J, Megha KB, Karthikeyan A, Gopinath N, Mohanan PV, Nair BG (2024) 3D printed arrowroot starch-gellan scaffolds for wound healing applications. Int J Biol Macromol 264:130604. https://doi.org/10.1016/j.ijbiomac.2024.130604
Ju F, Hua L, Wang R, Li T, Xu J, Bu H, Yang H (2025) Experimental and modeling assessment on the rheological behavior of collagen solutions modified by dibenzaldehydeterminated polyethylene glycol with different molecular weights. ACS Appl Polym Mater 7:13063–13075. https://doi.org/10.1021/acsapm.5c02312
Ju H, Liu X, Zhang G, Liu D, Yang Y (2020) Comparison of the structural characteristics of native collagen fibrils derived from bovine tendons using two different methods: modified acid-solubilized and pepsin-aided extraction. Materials 13(2):358. https://doi.org/10.3390/ma13020358
Kaczmarek-Szczepańska B, Polkowska I, Małek M, Kluczyński J, Paździor-Czapula K, Wekwejt M, Michno A, Ronowska A, Pałubicka A, Nowicka B, Otrocka-Domagała I (2023) The characterization of collagen-based scaffolds modified with phenolic acids for tissue engineering application. Sci Rep 13:9966. https://doi.org/10.1038/s41598-023-37161-6
Koski C, Bose S (2019) Effects of amylose content on the mechanical properties of starch-hydroxyapatite 3D printed bone scaffolds. Addit Manuf 30:100817. https://doi.org/10.1016/j.addma.2019.100817
Lai G, Li Y, Li G (2008) Effect of concentration and temperature on the rheological behavior of collagen solution. Int J Biol Macromol 42:285–291. https://doi.org/10.1016/j.ijbiomac.2007.12.010
Li Y, Yang L, Wu S, Chen J, Lin H (2022) Structural, functional, rheological, and biological properties of the swim bladder collagen extracted from grass carp (*Ctenopharyngodonidella*). LWT 153:112518. https://doi.org/10.1016/j.lwt.2021.112518
Liu X, Zheng C, Luo X, Wang X, Jiang H (2019) Recent advances of collagen-based biomaterials: multi-hierarchical structure, modification and biomedical applications. Mater Sci Eng C Mater Biol Appl 99:1509–1522. https://doi.org/10.1016/j.msec.2019.02.070
Lönroth EC, Dahl SE (2003) Cytotoxicity of liquidas and powers of chemically different dental materials evaluated using dimethylthiazoldiphenyl tetrazoliun and neutral red tests. Acta Odontol Scand 61(1):52–56. https://doi.org/10.1080/ode.61.1.52.56
Low SP, Williams KA, Canham LT, Voelcker NH (2006) Evaluation of mammalian cell adhesion on surface-modified porous silicon. Biomaterials 27:4538–4546. https://doi.org/10.1016/j.biomaterials.2006.04.015
Mandala IG, Savvas TP, Kostaropoulos AE (2004) Xanthan and locust bean gum influence on the rheology and structure of a white model-sauce. J Food Eng 64:335–342. https://doi.org/10.1016/j.jfoodeng.2003.10.018
Massimino LC, Martins VCA, Vulcani VAS, de Oliveira EL, Andreeta MB, Bonagamba TJ, Klingbeil MFG, Mathor MB, Plepis AMG (2020) Use of collagen and auricular cartilage in bioengineering: scaffolds for tissue regeneration. Cell Tissue Bank 25:111–122. https://doi.org/10.1007/s10561-020-09861-0
Masson-Meyers DS, Tabatabaei F, Steinhaus L, Toth JM, Tayebi L (2023) Development of fibroblast/endothelial cell-seeded collagen scaffolds for in vitro prevascularization. J Biomed Mater Res B Appl Biomater 111(3):633–645. https://doi.org/10.1002/jbm.b.35182
Matar GH, Andac M, Elmas A (2022) Locust bean gum-polyvinyl alcohol hydrogels: synthesis, characterization, swelling behaviors, and mathematical models. J Appl Polym Sci 139(3):e51498. https://doi.org/10.1002/app.51498
McGarry K, Sefat E, Suh TC, Ali KM, Gluck JM (2023) Comparison of NIH 3T3 cellular adhesion on fibrous scaffolds constructed from natural and synthetic polymers. Biomimetics 8(1):99. https://doi.org/10.3390/biomimetics8010099
Milan EP, Bertolo MRV, Martins VCA, Bogusz Junior S, Plepis AMG (2022a) Chitosan and collagen-based materials enriched with curcumin (*Curcuma longa*): rheological and morphological characterization. Polysaccharides 3:236–249. https://doi.org/10.3390/polysaccharides3010013
Milan EP, Martins VCA, Horn MM, Plepis AMG (2022b) Influence of blend ratio and Mangosteen extract in chitosan/collagen gels and scaffolds: rheological and release studies. Carbohydr Polym 292:119647. https://doi.org/10.1016/j.carbpol.2022.119647
Milan EP, Rodrigues MAV, Martins VCA, Plepis AMG, Fuhrmann-Lieker T, Horn MM (2021) Mineralization of phosphorylated fish skin collagen/Mangosteen scaffolds as potential materials for bone tissue regeneration. Molecules 26:2899. https://doi.org/10.3390/molecules26102899
Montalbano G, Calore AR, Vitale-Brovarone C (2023) Extrusion 3D printing of a multiphase collagen-based material: an optimized strategy to obtain biomimetic scaffolds with high shape fidelity. J Appl Polym Sci 140(10):e53593. https://doi.org/10.1002/app.53593
Moshayedi S, Sarpoolaky H, Khavandi A (2021) Fabrication, swelling behavior, and water absorption kinetics of genipin-crosslinked gelatin–chitosan hydrogels. Polym Sci Eng 61(12):3094. https://doi.org/10.1002/pen.25821
Moss SP, Shiwarski DJ, Feinberg AW (2025) FRESH 3D bioprinting of collagen types I, II, and III. ACS Biomater Sci Eng 11(1):556–563. https://doi.org/10.1021/acsbiomaterials.4c01826
Munhoz MAS, Hirata HH, Plepis AMG, Martins VCA, Cunha MR (2018) Use of collagen/chitosan sponges mineralized with hydroxyapatite for the repair of cranial defects in rats. Injury 49:2154–2160. https://doi.org/10.1016/j.injury.2018.09.018

Nik WWB, Ani FN, Masjuki HH, Giap SGE (2005) Rheology of bio-edible oils according to several rheological models and its potential as hydraulic fluid. Ind Crop Prod 22:249–255. https://doi.org/10.1016/j.indcrop.2005.01.005

Nocera AD, Comín R, Salvatierra NA, Cid MP (2018) Development of 3D printed fibrillar collagen scaffold for tissue engineering. Biomed Microdevices 20:26. https://doi.org/10.1007/s10544-018-0270-z

Normah I, Afiqah MM (2018) Effect of extraction time on the physicochemical characteristics of collagen from sin croaker (*Johniecop sina*) waste. Int Food Res J 25(3):1074–1080

Pei M, Hwangbo H, Kim GH (2023) Hierarchical fibrous collagen/poly(ε-caprolactone) structure fabricated with a 3D-printing process for tissue engineering applications. Compos Part B Eng 259:110730. https://doi.org/10.1016/j.compositesb.2023.110730

Perez RA, Mestres G (2016) Role of pore size and morphology in musculo-skeletal tissue regeneration. Mater Sci Eng C Mater Biol 61:922–939. https://doi.org/10.1016/j.msec.2015.12.087

Putri NRE, Wang X, Chen Y, Li X, Kawazoe N, Chen G (2020) Preparation of PLGA-collagen hybrid scaffolds with controlled pore structures for cartilage tissue engineering. Prog Nat Sci Mater Int 30:642–650. https://doi.org/10.1016/j.pnsc.2020.07.003

Razavi SMA, Cui SW, Ding H (2016) Structural and physicochemical char- acteristics of a novel water-soluble gum from *Lallemantia royleana* seed. Int J Biol Macromol 83:142–151. https://doi.org/10.1016/j.ijbiomac.2015.11.076

Razmkhah S, Razavi SMA, Mohammadifar MA (2017) Dilute solution, flow behavior, thixotropy and viscoelastic characterization of cress seed (*Lepidium sativum*) gum fractions. Food Hydrocolloids 63:404–413. https://doi.org/10.1016/j.foodhyd.2016.09.030

Shatwell KP, Sutherland IW, Ross-Murphy SB, Dea ICM (1991) Influence of the acetyl substituent on the interaction of xanthan with plant polysaccharides - I. xanthan-locust bean gum systems. Carbohydr Polym 14:29–51. https://doi.org/10.1016/0144-8617(90)90005-D

Song P, Zhou C, Fan H, Zhang B, Pei X, Fan Y, Jiang Q, Bao R, Yang Q, Dong Z (2018) Novel 3D porous biocomposite scaffolds fabricated by fused deposition modeling and gas foaming combined technology. Compos Part B Eng 152:151–159. https://doi.org/10.1016/j.compositesb.2018.06.029

Sponchiado PAI, de Melo MT, Bitencourt BS, Guedes JS, Tapia-Blácido DR, Augusto PED, Ramos AP, Maniglia BC (2024) Clean modification of potato starch to improve 3D printing of potential bone bio-scaffolds. Emergent Mater 8(4):2695–2708. https://doi.org/10.1007/s42247-024-00673-6

Sukumaran A, Sweety VK, Vikas B, Joseph B (2023) Cytotoxicity and cell viability assessment of biomaterials. IntechOpen. https://doi.org/10.5772/intechopen.111822

Sun L, Li B, Yao D, Song W, Hou H (2018) Effects of crosslinking on mechanical, biological properties and biodegradation behavior of Nile Tilapia skin collagen sponge as a biomedical material. J Mech Behav Biomed Mater 80:51–58. https://doi.org/10.1016/j.jmbbm.2018.01.006

Tang H, Zhou W, Zhang L (2012) Adsorption isotherms and kinetics studies of malachite green on chitins. J Hazard Mater 209:218–225. https://doi.org/10.1016/j.jhazmat.2012.01.010

Trębacz H, Szczęsna A, Arczewska M (2018) Thermal stability of collagen in naturally ageing and in vitro glycated rabbit tissues. J Therm Anal Calorim 134(3):1903–1911. https://doi.org/10.1007/s10973-018-7375-8

Vagaská B, Bacáková L, Filová E (2010) Osteogenic cells on bio-inspired materials for bone tissue engineering. Physiol Res 59(3):309–322. https://doi.org/10.33549/physiolres.931776

Vargas-Rodríguez YM, Obaya A, García-Petronilo JE, Vargas-Rodríguez GI, Gómez-Cortés A, Tavizón G, Chávez-Carvayar JA (2021) Adsorption studies of aqueous solutions of methyl green for halloysite nanotubes: kinetics, isotherms, and thermodynamic parameters. Am J Nanomater 9(1):1–11. https://doi.org/10.12691/ajn-9-1-1

Wang Y, Wang Z, Dong Y (2023) Collagen-based biomaterials for tissue engineering. ACS Biomater Sci Eng 9:1132–1150. https://doi.org/10.1021/acsbiomaterials.2c00730

Xie R, Pal V, Yu Y, Lu X, Gao M, Liang S, Huang M, Peng W, Ozbolat IT (2024) A comprehensive review on 3D tissue models: biofabrication technologies and preclinical applications. Biomaterials 304:122408. https://doi.org/10.1016/j.biomaterials.2023.122408

Yadav P, Beniwal G, Saxena KK (2021) A review on pore and porosity in tissue engineering. Mater Today Proc 44:2623–2628. https://doi.org/10.1016/j.matpr.2020.12.661

Yang H, Duan L, Li Q, Tian Z, Li G (2018) Experimental and modeling investigation on the rheological behavior of collagen solution as a function of acetic acid concentration. J Mech Behav Biomed Mater 77:125–134. https://doi.org/10.1016/j.jmbbm.2017.09.003

Yang X, Yang D, Lin X, Li D, Shi W, Xiang Z, Mu C, Ge L, Li D, Xu Z (2023) Effect of dehydrothermal treatment on the structure and properties of a collagen-based heterogeneous bilayer membrane. ACS Appl Polym Mater 5:3427–3438. https://doi.org/10.1021/acsami.5c18404

Zhang M, Chen Y, Li G, Du Z (2010) Rheological properties of fish skin collagen solution: effects of temperature and concentration. Korea-Aust Rheol J 22(2):119–127

Zhang Z, Feng Y, Wang L, Liu D, Qin C, Shi Y (2022) A review of preparation methods of porous skin tissue engineering scaffolds. Mater Today Commun 32:104109. https://doi.org/10.1016/j.mtcomm.2022.104109

Zhang Z, Li G, Shi B (2005) Physicochemical properties of collagen, gelatin and collagen hydrolysate derived from bovine limed split wastes. J Soc Leather Technol Chem 90:23–28

Zhao XR, Xu X, Teng J, Zhou N, Zhou Z, Jiang XY, Jiao FP, Yu JG (2019) Threedimensional porous graphene oxide-maize amylopectin composites with controllable pore-sizes and good adsorption-desorption properties: facile fabrication and reutilization, and the adsorption mechanism. Ecotoxicol Environ Saf 176:11–19. https://doi.org/10.1016/j.ecoenv.2019.03.069